remote sensing

Article

IonosphericTotal Electron Content Changes during the 15 February 2018 and 30 April 2022 Solar Eclipses over South America and Antarctica

Juan Carlos Valdés-Abreu [1,2], Marcos Díaz [1,2,*], Manuel Bravo [3] and Yohadne Stable-Sánchez [1]

[1] Space and Planetary Exploration Laboratory (SPEL), Faculty of Physical and Mathematical Sciences, University of Chile, Av. Tupper 2007, Santiago 8370451, Chile; juanvaldes@ug.uchile.cl (J.C.V.-A.); spel@ing.uchile.cl (Y.S.-S.)
[2] Department of Electrical Engineering, Faculty of Physical and Mathematical Sciences, University of Chile, Av. Tupper 2007, Santiago 8370451, Chile
[3] Centro de Instrumentación Científica, Universidad Adventista de Chile, km 12 Camino a Tanilvoro, Chillan 3780000, Chile; manuelbravo@unach.cl
* Correspondence: mdiazq@ing.uchile.cl

Abstract: This is one of the first papers to study the ionospheric effects of two solar eclipses that occurred in South America and Antarctica under geomagnetic activity in different seasons (summer and autumn) and their impact on the equatorial ionization anomaly (EIA). The changes in total electron content (TEC) during the 15 February 2018 and 30 April 2022 partial solar eclipses will be analyzed. The study is based on more than 390 GPS stations, Swarm-A, and DMSP F18 satellite measurements, such as TEC, electron density, and electron temperature. The ionospheric behaviors over the two-fifth days on both sides of each eclipse were used as a reference for estimating TEC changes. Regional TEC maps were created for the analysis. Background TEC levels were significantly higher during the 2022 eclipse than during the 2018 eclipse because ionospheric levels depend on solar index parameters. On the days of the 2018 and 2022 eclipses, the ionospheric enhancement was noticeable due to levels of geomagnetic activity. Although geomagnetic forcing impacted the ionosphere, both eclipses had evident depletions under the penumbra, wherein differential vertical TEC (DVTEC) reached values $<-40\%$. The duration of the ionospheric effects persisted after 24 UT. Also, while a noticeable TEC depletion (DVTEC $\sim-50\%$) of the southern EIA crest was observed during the 2018 eclipse (hemisphere summer), an evident TEC enhancement (DVTEC $> 30\%$) at the same crest was seen during the eclipse of 2022 (hemisphere autumn). Swarm-A and DMSP F18 satellite measurements and analysis of other solar eclipses in the sector under quiet conditions supported the ionospheric behavior.

Keywords: ionosphere; solar eclipse; global positioning system (GPS); satellite measurements; total electron content (TEC); in situ measurements; equatorial ionization anomaly

Citation: Valdés-Abreu, J.C.; Díaz, M.; Bravo, M.; Stable-Sánchez, Y. Ionospheric Total Electron Content Changes during the 15 February 2018 and 30 April 2022 Solar Eclipses over South America and Antarctica. *Remote Sens.* **2023**, *15*, 4810. https://doi.org/10.3390/rs15194810

Academic Editor: Fabio Giannattasio

Received: 26 July 2023
Revised: 30 August 2023
Accepted: 4 September 2023
Published: 3 October 2023

1. Introduction

The ionospheric TEC changes can be provoked by some sources, such as solar flares, geomagnetic storms, solar eclipses, solar terminators, tropical cyclones, thunderstorms/lightning, volcanic eruptions, earthquakes, tsunamis, and rocket launches, among others [1,2]. These ionospheric disturbance sources can cause blackouts in radio signals and are an important problem for satellite communication and radionavigation systems [2].

Solar eclipses provide a unique opportunity to investigate atmospheric and ionospheric processes from the Earth's surface to the topside ionosphere during the fast sunlight–umbra transitions and vice versa. During solar eclipses, solar radiation is attenuated because it is partially blocked by the Moon. Consequently, the sudden decreases in photo-ionization and photo-electron heating of solar extreme ultraviolets (EUVs) affect all the ionospheric layers [3]. This results in the loss of plasma and a local drop in electron density (N_e) dominating the output rate on an eclipse day relative to a regular day.

The total electron content (TEC in TECu, where 1 TECu $= 10^{16}$ el/m^2) is a measure of N_e in the ionosphere integrated along the line of sight; therefore, it provides accurate information about ionization behavior. During eclipses, the TEC fluctuates and can be characterized by the amplitude as differential TEC (in TECu and/or %), which usually has a reduction; delay value (τ in min) relative to the maximum obscuration time (MOT) of the eclipse; and duration (ΔT in hours) of the disturbance [1]. TEC can be estimated via a radio link between Earth and space. The Global Navigation Satellite System (GNSS) is the most widely used communication system for estimating TEC in the ionosphere. Therefore, we use the Global Positioning System (GPS) in this work, which is one of the constellations of satellites that make up GNSS.

The solar eclipse-induced effects on the ionosphere are not simply local, but can even influence areas outside the eclipse's shadow. These effects may be caused by the transfer of hemisphere magnetic conjugates, changes in the equatorial vertical E $\times$ B drift, the development of a disturbance dynamo, and atmospheric gravity waves (AGWs) that generate traveling ionospheric disturbances (TIDs) and/or traveling atmospheric disturbances (TADs) [4–16]. The supersonic moving shadow of solar eclipses on Earth's atmosphere can cause AGWs. Furthermore, the existence of eclipse waves (AGWs, TADs, and TIDs) affects a number of systems, including radiocommunication, radionavigation, and geolocalization.

Ionospheric effects during high-latitude eclipses are driven by intense ionosphere–magnetosphere coupling, particularly during high levels of geomagnetic activity [17–19]; while ionospheric effects during low-latitude eclipses are influenced by electrodynamics processes associated with the equatorial ionization anomaly (EIA) [20,21]. The equatorial vertical E $\times$ B drift, which induces plasma transfer from the magnetic equator to the crest area and decreases strongly during solar eclipses, as has been seen, for example, during the 4 October 1995 and the 9 March 1997 solar eclipses [22]. It has been seen that the EIA source effect is frequently suppressed during Sun–Earth–Moon alignments (full moon, new moon, and eclipse), even with evidence of equatorial counter-electrojets during solstices [23–26]. On the other hand, depending on the geometric configuration of the eclipse and season of occurrence, it can increase or decrease the EIA crests separately, generating asymmetry. Additionally, Resende et al. [27] showed a summary of current studies that found EIA crests decreasing during solar eclipse occurrences, where TEC decrease was between -50% and -20% in comparison to the background ionosphere. In contrast, some authors found TEC increases around the EIA (e.g., [28–31]). For instance, Chen et al. [29] proved that eclipse-induced wind and temperature may significantly influence the ionospheric enhancement at EIA crests. Moreover, the dynamic processes that occur during a single eclipse are heavily influenced by the eclipse trajectory, time of day, location, synoptic, seasons, geomagnetic conditions, geophysical conditions, and solar variation [15,32]. The trajectories of an eclipse can differ geographically and temporally depending on the observing altitude chosen, which could be important for researching ionospheric dynamics. Research has shown the importance of estimating the eclipse mask at the height of the ionosphere to be studied and not only working with the mask at the surface level [33–35].

Recently, several authors published TEC variations and observed anomalies related to solar eclipses in various geographic locations. Kundu et al. [36] presented the change in ionospheric plasma density during the annular solar eclipse on 26 December 2019, through multi-directional approaches by using ground-based TEC and space-based Swarm satellite and observed a depletion in TEC and N_e that is directly proportional to the solar obscuration function. Several authors have used different instruments (mainly VLF receivers) and computed N_e variation using LWPC simulation also [37–40]. Including ionospheric responses to the partial and annular eclipse in different regions will help the reader to make comparisons with other cases and results obtained from other instruments.

The partial solar eclipses of 15 February 2018 (PSE2018) and 30 April 2022 (PSE2022) were the first eclipses of 2018 and 2022, respectively. These eclipses were visible from over parts of Antarctica, the Pacific, and the Atlantic Oceans. Moreover, both eclipses were observed over southern South America in the afternoon (http://xjubier.free.fr/en/site_pages/SolarEclipsesGoogleMaps.html, last accessed on 20 August 2023). PSE2018 and PSE2022 happened over days with some levels of geomagnetic activity. Therefore, these two partial solar eclipses offer an excellent opportunity to study their effects on the regional ionosphere, under different geometric configurations of the eclipse and season of occurrence.

Recent studies looked at the ionospheric effects of solar eclipses over South America and Antarctica. The 2 July 2019 total solar eclipse (TSE2019) occurred in the southern hemisphere winter (subsolar latitude ∼23°N) from 16.92 UT to 21.83 UT. TEC showed clear decreases (−40% to −25%) compared to the background ionosphere and a 57% rise near the southern EIA crest. TIDs presented wavelengths ranging from approximately 100 km to more than 200 km, with periods between 20 and 50 min. Jonah et al. [10,31] reported a TEC enhancement effect that altered the equatorial electrodynamics. Jonah et al. [31] utilized an incoherent scatter radar in Jicamarca and 2500 GNSS stations localized over South and North America. Maurya et al. [10] studied 24 Chilean GPS station datasets localized north and south to the path of totality. The wavelet analysis of the VTEC time series showed the presence of strong AGWs of duration from 30 to 60 min at the GPS stations located the north of totality. Aryal et al. [41] used NASA's Global-scale Observation of Limb and Disk (GOLD) instrument aboard the SES-14 satellite in a geostationary orbit. They reported an important decrease in brightness around totality in OI 135.6 nm and N2 LBH band emissions when compared to baseline observations taken two days earlier. They also observed a large increase in the ΣO/N2 column density ratio (∼80%) within the totality of the eclipse. Vargas et al. [42] presented the Andes Lidar Observatory (ALO), TIMED/SABER temperatures, and ionosonde electron density measurements. Bravo et al. [43] used an ionosonde within the totality path and ∼500 GNSS receivers localized over South America, which were compared with two ionosonde measurements. The authors modeled the ionospheric effects in the Sheffield University Plasmasphere-Ionosphere Model (SUPIM). Also, they corroborated the relationship between diminishing solar radiation with densities below 200 km and the E and F1 layer critical frequencies. Eisenbeis and Occhipinti [6] analyzed TEC depletion and applied the omega-k technique, which was based on a 3D Fast Fourier Transform. Yan et al. [15] simulated in the Thermosphere-Ionosphere-Electrodynamics General Circulation Model (TIE-GCM) the thermospheric perturbations induced by four different eclipses, such as TSE2019. TADs are induced by fast-moving shadows form bow wavefronts during the eclipse and evolve into freely propagating large-scale TADs after the eclipse ends. During TSE2019, TADs propagated in a direction with a smaller solar zenith angle that deviated from the eclipse trajectory.

The 14 December 2020 total solar eclipse (TSE2020) took place in the southern hemisphere summer (subsolar latitude ∼23°S) between 13.56 UT and 18.88 UT, and its geographic location was similar to TSE2019. The DVTEC values had −40% to −20% in the penumbra compared to the background TEC during TSE2020. Therefore, TSE2020 had similar ionospheric values to the values obtained for TSE2019. On average, the maximum dimming occurred 20 to 30 min after MOT of the eclipse at the location of the GPS stations. However, the southern EIA crest was characterized by an ionospheric decrease (DVTEC between −50% to −30%) during TSE2020, as opposed to TSE2019. Previously, Martinez et al. [44] used SUPIM, and were the first to anticipate the ionospheric effect due to TSE2020. They modified the SUPIM to simulate the behavior of solar obscuration on the ionosphere at low and middle magnetic latitudes. Gómez [45] compared TEC variations using 46 GNSS stations around the path of the umbra of the eclipse to that predicted by the SAMI3. The results showed that TEC perturbations after totality could be triggered by orographic gravity waves (oGWs) not related to the eclipse. The passage of TSE2020 across the Andes Mountains aided the propagation of orographic gravity waves to ionospheric heights. Meza et al. [11] simultaneously analyzed the ionospheric and geomagnetic responses to TSE2020. They used data from GNSS stations located in the Argentine and Chilean sectors. The authors analyzed the relationship between VTEC and geomagnetic changes. Resende et al. [27] analyzed the effects of TSE2020 over the Brazilian sector using two digisonde data sources, GNSS-TEC, and the MIRE numerical model. Additionally, de Haro Barbás et al. [46] analyzed eclipse effects on critical ionospheric frequency variability, considering two ionosondes with similar geographical latitudes and a 95% obscuration percentage. They also compared the ionospheric response with the IRI-2016 model. Shrivastava et al. [13] used 36 Chilean GPS stations localized across both sides of the totality line. Although they observed strong AGWs at the GPS stations located north of the path of totality, the AGWs had no noticeable impact on the VTEC of these sites. They found the presence of large variability in the background VTEC values during TSE2020. The authors also compared the ionospheric effects of TSE2019 and TSE2020. Zhang and Wang et al. [47] examined the space-based measurements (Swarm-B/C, COSMIC, and ICON/MIGHTI missions) of equatorial electrojet, zonal winds, and N_e for TSE2020. They reported the evident decrease in equatorial electrojet ($<-29\%$) during the solar eclipse, in comparison with non-eclipse. Recently, Bravo et al. [48] used data from multiple instruments (ionosondes, an Incoherent Scatter Radar, GNSS stations, and GOLD and Swarm-A missions) to evaluate the ionospheric prediction for a solar eclipse over South America conducted by [44]. Bravo et al. [48] also compared the predictions with three different GNSS-TEC estimation methods. Furthermore, they contrasted their evaluation's findings with earlier studies of the ionospheric behavior of TSE2019 and TSE2020.

Over Antarctica, there was a total solar eclipse on 4 December 2021 (TSE2021). The zone of the penumbral eclipse covered Antarctica and was observed over small southernmost sections of southern South America, Africa, New Zealand, and Australia between 5.48 UT and 9.62 UT. Idosa and Rikitu [49] studied TEC effects due to TSE2021 at six GPS stations in Antarctica. Over the six stations, the TEC value decreased during the eclipse. DVTEC values during the eclipse were about −70% to −50% around 8 UT (in the daytime), and in the nighttime, TEC enhancements were about 30% to 150%. The maximum TEC enhancement was at all sites after the eclipse day. Coyle et al. [50] compared GPS TEC observations to the TIE-GCM model ionosphere. They used ground magnetometer observations located along the 40° magnetic meridian between 69°S and 79°S and their magnetically conjugate counterpart. They observed a substorm that took place one hour prior to peak totality in the AE index and in the combined array magnetograms. The results showed that TEC frequency oscillations were similar to the magnetometer data. The authors' analyses suggested that these observations were caused by eclipse effects rather than the substorm.

In a recent study, Idosa and Beshir [51] reported the TEC variations during the PSE2022 using three GPS stations localized in Santiago (33.44°S, 70.67°W), Montevideo (34.90°S, 56.16°W), and Falkland (51.45°S, 59.00°W). On the day of the eclipse, prior to the event, it was possible to observe that DVTEC at the three GPS stations reached values greater than 30%. According to their study, the GPS station they used with the highest percentage of obscuration was localized in Santiago (MPO 28% at sea level). During the eclipse, the DVTEC experienced deviations from the background ionosphere over Santiago (−39%), Montevideo (−29%), and Falkland (−60%). Finally, the authors used the three stations to compare the TEC behavior due to the 14 April 2022 moderate geomagnetic storm and PSE2022. They concluded that the TEC response to the analyzed storm was greater than that of the PSE2022-induced effects on the ionosphere. Then, Idosa and Beshir [51] did not present TEC maps or the ionospheric effects of the 2022 partial eclipse on the EIA.

Additionally, some studied eclipses have occurred on days when the geomagnetic field has been at active levels, such as the total solar eclipses of 23 November 2003 and 20 March 2015. Both eclipses happened over polar regions. The eclipse of 2003 happened over Antarctica, during the recovery phase of the great storm on 20 November 2003. Over the partial zone of this eclipse, TEC levels at the time window of the eclipse were about −30% to −17% with respect to the day before and the day after the eclipse, respectively [52]. The eclipse of 20 March 2015 took place across Arctic regions, during the recovery phase of the 2015 St. Patrick's geomagnetic storm that started a few days earlier (2015 March 17), and it was accompanied by a negative ionospheric storm on 20 March 2015. Despite the geomagnetic activity, numerous studies have documented ionospheric changes (DVTEC between $\sim-50\%$ and -10%) caused by the eclipse of 20 March 2015 relative to the background (e.g., [14,53–56]).

In this paper, we study and compare the effects of PSE2018 and PSE2022 on TEC behavior over South America and Antarctica regions. We also take this opportunity to analyze the ionospheric effects induced by both solar eclipses on the EIA. The analysis is based on more than 390 GPS stations (see Figure 1), Swarm-A satellite (SwA) of the European Space Agency's Swarm mission, and DMSP 5D-3 F18 spacecraft (F18) of the Defense Meteorological Satellite Program (DMSP). Our study is relevant because sources of ionospheric disturbances are a significant issue for space-based communication and radionavigation systems. Due to the fact that GPS is a radio-link-based technology, it can be affected by ionospheric fluctuations. Furthermore, our results were compared with previous studies about the ionospheric response to TSE2019, TSE2020, and TSE2021. We must emphasize that this is one of the first works where the ionospheric behavior due to two eclipses that occurred in South America and Antarctica under geomagnetic activity and in different seasons of the year are studied and compared, as well as the ionospheric effects that both eclipses had on the behavior of the EIA.

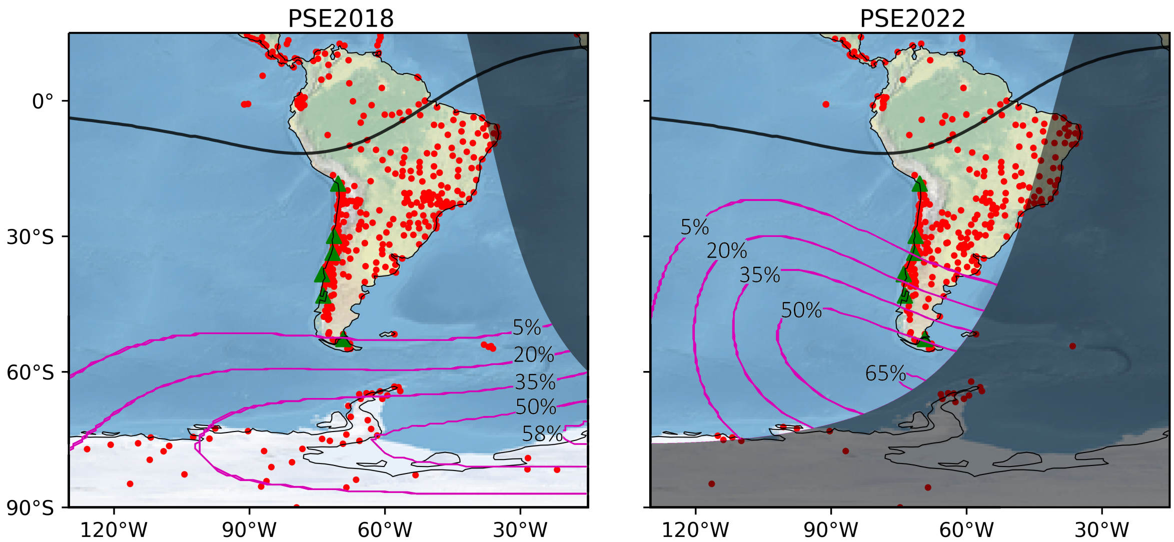

Figure 1. GPS stations (red dots) and six selected GPS stations (green triangles) used in present work. Eclipse obscuration masks at 350 km altitude (magenta lines) at Greatest Eclipse (GE) time, and the magnetic equator (black line) are also shown. The 507 and 398 GPS stations were used in PSE2018 (**left panel**) and PSE2022 (**right panel**), respectively.

2. Materials and Methods

Our study of PSE2018 and PSE2022 is based partially on the methodology described in [2,34,57]. We used the approach proposed in [35] to determine the eclipse masks at 350 km ionospheric height. This work's technique also involves an examination of geophysical and geomagnetic conditions near the dates of two eclipses (15 February 2018, and 30 April 2022). Below, we describe how we work with these data.

2.1. Brief Information about PSE2018 and PSE2022

PSE2018 had its first external contact (P1) at 18.93 UT and its last external contact (P4) at 22.79 UT. Its maximum magnitude was 0.60 at geographic coordinates 71.03°S, and 0.64°W, at 20.86 UT (Greatest Eclipse, GE). The 2018 eclipse happened in the southern hemisphere summer (subsolar latitude $\sim$12°S).

While P1 and P4 time of PSE2022 were at 18.75 UT and 22.63 UT, respectively, their maximum magnitude was 0.64 at geographic coordinates 62.12°S, and 71.48°W, at GE time equal to 20.69 UT. The 2022 eclipse occurred during the southern hemisphere autumn (subsolar latitude ∼15°N).

Eclipse obscuration masks at 350 km altitude are shown in Figure 1, in accordance with the method suggested by Verhulst et al. [35]. On 15 February 2018, the Sun was hidden by the Moon at a maximum percentage of obscuration (MPO) of about 60% over Antarctica at 350 km altitude, while on 30 April 2022, at its peak, the Moon covered 66% of the Sun's disk at 350 km altitude.

Moreover, the maximum percentages of obscuration over South America were observed over Puerto Williams due to the trajectories of the two analyzed eclipses. The maximum percentages of obscuration at 350 km altitude caused by PSE2018 and PSE2022 over this city were 35% at 21.62 UT and 63% at 20.98 UT, respectively. Puerto Williams (54.9°S, 67.7°W) is a city in southern Chile, South America. It is called the world's southernmost city.

2.2. Estimation of the Ionospheric TEC

We evaluated the period of days around both eclipses (±5 days compared to the eclipse day). We imposed several conditions for the selection of reference days. First, the geomagnetic conditions for an entire day had to have quiet levels (Kp $\leq 2^+$, Dst > -30 nT), as well as the Bz component of the interplanetary magnetic field (|IMF-Bz| $\leq$ 10 nT) and the solar wind speed (Vsw $<$ 450 km/s) conditions (see Section 2.4). Second, the days chosen had to have the closest trajectories of the two satellites (SwA and F18) with respect to each eclipse day, both longitudinally and temporally. Third, we wanted to preserve the symmetry of days with regard to the eclipse's day, even though this is less important than the two previous points. Therefore, we worked with the eclipse day, and we took the fifth day before and the fifth day after the eclipse as reference days.

Using the GPS-TEC analysis program version 2.9.5, we estimated the vertical TEC (VTEC) at 350 km altitude from RINEX observation files of the dual-frequency signals (f_1 and f_2) (https://seemala.blogspot.com, last accessed on 25 July 2023) [58] wherein two types of delay are continuously recorded by the dual-frequency GPS receiver: the carrier phases and the pseudoranges of the f_1 and f_2. The acquired data were then utilized to determine the slant TEC (STEC) and VTEC. To limit potential errors, we calculated the VTEC values at a 350 km ionospheric height with a 30° satellite elevation angle as the cut-off (ionospheric pierce point, IPP). TEC values are delivered by software every 30 s and are corrected for receiver and satellite bias using the data obtained from the Center for Orbit Determination in Europe (CODE) (ftp://ftp.aiub.unibe.ch/CODE, last accessed on 25 July 2023).

We evaluated the quality of the files on the chosen days for each GNSS station before making the final selection of its RINEX files. In order to ensure high-quality data, we preprocessed the RINEX observation files using TEQC software (version of 25 February 2019, https://www.unavco.org, last accessed on 20 August 2023) [59]. We made sure that the 24 h RINEX observation files with 30 s intervals were complete and of good quality. For example, we discarded GNSS stations wherein files had general RINEX formatting issues, truncated files, and the like. Also, we verified that there were no errors or data gaps after TEC estimation. This quality checking is critical to making a good comparison of the ionospheric TEC changes between the chosen days. The Chilean network set up by the National Seismological Center (CSN in Spanish); the Argentine network (RAMSAC) [60]; the Brazilian network (RBMC); and UNAVCO provided RINEX files of more than 390 GPS stations that fulfilled our specifications (see Figure 1). This study mainly focused on the South American and Antarctic regions. Then, we used 507 and 398 GPS stations used in PSE2018 (see Figure 1 left panel) and PSE2022 (see Figure 1 right panel), respectively.

Additionally, we use differential VTEC (DVTEC in TECu and %) to analyze ionospheric irregularities, as shown in Equations (1) and (2) [34,57,61].

$$DVTEC_t = VTEC_t - \overline{VTEC_t} \quad (1)$$

$$DVTEC[\%]_t = \frac{DVTEC_t}{\overline{VTEC_t}} \cdot 100 \quad (2)$$

where the mean value of VTEC ($\overline{VTEC_t}$) at the same time of the day, and t represents the epoch. Also, $\overline{VTEC_t}$ is calculated using the reference days, Days of Year (DoYs) 41 and 51, which correspond to the fifth day before and fifth day after the day of the eclipse (DoY 45) the day of the eclipse in 2018. In the same way, if DoY 120 was the day of the eclipse in 2022, we used as reference DoYs 115 and 125.

To represent the ionospheric TEC maps, we take all the VTEC values at IPPs at 350 km altitude within a range of 2.5° latitude and 2.5° longitude (starting from the Geographic Equator) and average them to generate a single VTEC value within a spatial resolution of 2.5° × 2.5° and temporal resolution of 2 min. Furthermore, to correctly carry out the algebra of maps using Equations (1) and (2), we only consider the quadrants (2.5° × 2.5°) that show values during all the days analyzed (reference days and eclipse days) at the same time of the day for each eclipse.

2.3. Ionospheric Observations and Satellite Measurements

We used ionospheric observations obtained from SwA and F18 satellites. We analyzed the eclipse-induced local ionospheric reactions using numerous space-based measurements, such as VTEC, in situ N_e, and electron temperature (T_e) data provided by SwA. This satellite has an inclination of 88° and a circular orbit at about 450 km height over the sea level. We also used in situ N_e measurements provided by F18 in the topside ionosphere at about 850 km height over the sea level with an inclination of 99° and a circular orbit. The measurements from these satellites help us to corroborate the observations on the EIA crests at 350 km, although with different amplitudes since the measurements above 850 km correspond to the plasmasphere.

2.4. Geomagnetic and Geophysical Conditions

The 15 February 2018 (see left panel of Figure 2) and 30 April 2022 partial solar eclipses (see right panels of Figure 2) took place during days with geomagnetically active levels. We downloaded geomagnetic data from OMNIWeb Plus Data (https://omniweb.gsfc.nasa.gov, last accessed on 20 August 2023) and World Data Center (WDC) for Geomagnetism, Kyoto (http://wdc.kugi.kyoto-u.ac.jp, last accessed on 20 August 2023) [62]. Figure 2, from top to bottom, illustrates the 10.7 cm solar radio flux index (F10.7 in 1 sfu = 10^{-22} W/m^2/Hz), Kp index, Dst index (in nT), IMF-Bz (in nT), auroral electrojet index (AE in nT), Vsw (in km/s), and solar wind plasma temperature (Tsw in K) which characterize the geomagnetic conditions during DoYs 41 to 52 of 2018 and DoYs 115 to 126 of 2022.

Figure 2 (left panels) shows F10.7 with 66.3 to 76.6 sfu during DoYs 46 to 51 of 2018. The geomagnetic field presented active levels between DoYs 46 and 51. The maximum 3-h Kp was 5^- on DoY 46. Dst peak and maximum AE were −28 nT and 618 nT, respectively. IMF-Bz reached values from −5.6 to 11.7 nT. Vsw had ≥450 km/s (intermediate speeds) between DoYs 48 and 51, with a peak of 619 km/s. Tsw $> 100 \times 10^3$ K; DoYs 48 to 51 with a maximum equal to 252×10^3 K. Additionally, solar activity showed very low levels during DoYs 46 to 51.

On 15 February 2018, the geomagnetic conditions were at quiet to active levels (see Figure 2 (left panels)). The variations in 3-hourly Kp, Dst, the southward component of Bz, AE, and Vsw reached peak levels of 5^-, −18 nT, −4.2 nT, 495 nT, and 383 km/s between 15 UT and 18 UT. The maximum Tsw was 66×10^3 K at 13 UT. Also, the AE index was greater than 300 nT from 16 UT to 18 UT, and from 22 UT to 23 UT.

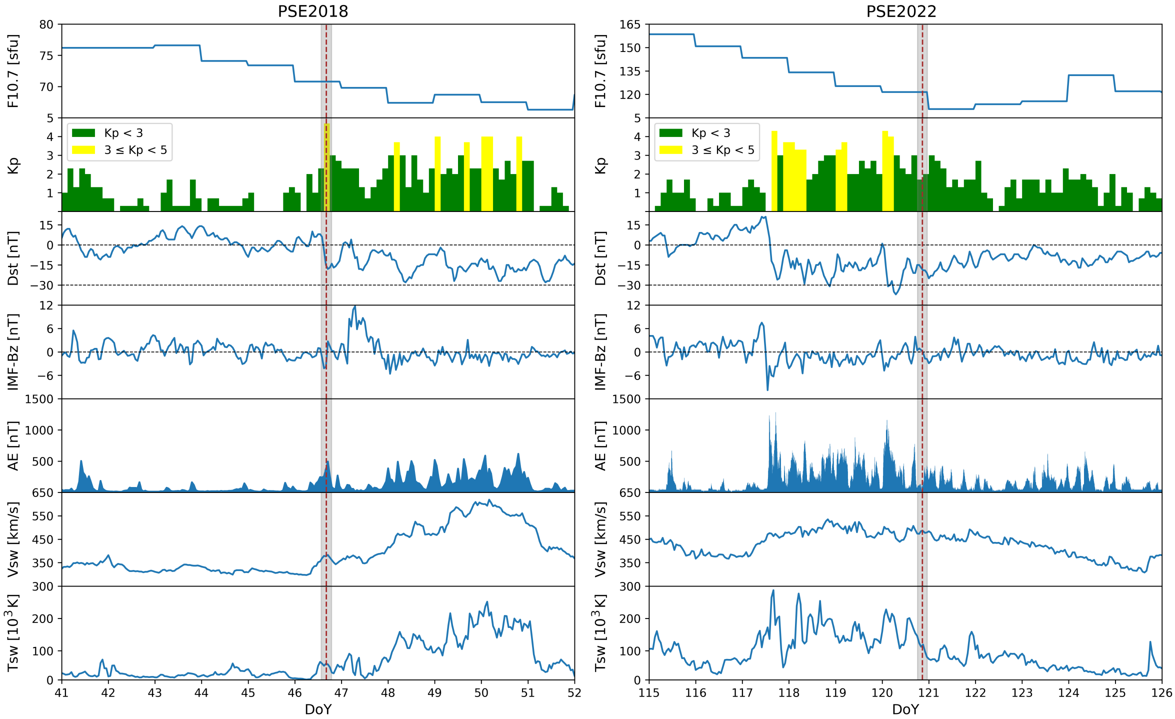

Figure 2. From top to bottom: F10.7, Kp, Dst, IMF-Bz, AE, Vsw, and Tsw used to describe geomagnetic conditions on DoYs 41 to 52 of 2018 (**left panel**) and on DoYs 115 to 126 of 2022 (**right panel**). GE (red dashed line) and P1 to P4 (light grey bar) are shown.

Figure 2 (right panels) illustrates F10.7 with 110.6 to 158.5 sfu during DoYs 115 to 126 of 2022. The geomagnetic field showed active levels between DoYs 117 and 123. The maximum 3-h Kp was 5. Dst showed a weak geomagnetic storm with −37 nT on DoY 120 (day of the 2022 eclipse). IMF-Bz reached values from −9.8 to 7.5 nT. AE presented values greater than 500 nT between DoYs 117 to 121, and it also had some values greater than 1000 nT during those days. Vsw had ≥450 km/s (intermediate speeds) between DoYs 117 and 123, with a peak of 535 km/s on DoY 118. Tsw $> 100 \times 10^3$ K; DoYs 48 to 51 with a maximum equal to 252×10^3 K.

On 30 April 2022, the geomagnetic conditions had quiet to minor storm levels (see right panel of Figure 2). There was a weak geomagnetic storm with a Dst peak equal to −37 nT at 8 UT (Dst ≤ -30 nT from 4 UT to 11 UT). The variations in 3-hourly Kp, the southward component of Bz, and Tsw reached peak values of 4^+, −4.8 nT, and 228×10^3 K between 0 UT and 3 UT. Vsw had intermediate speeds with a maximum of 503 km/s at 1 UT, and its peak equal to 507 km/s at 16 UT. Additionally, AE index was greater than 300 nT from 0.5 UT to 11.5 UT (AE > 500 nT, 0.5 to 7 UT), from 15 UT to 17.2 UT (AE > 500 nT, 16 to 17 UT), and from 21.5 to 23.5 UT. Solar activity presented high levels during the 24 h. Also, Active Region 2994 produced an X1.1 solar flare at 13.78 UT.

We should note that minor geomagnetic activities cannot be ignored because they sometimes play crucial roles in ionosphere plasma density, according to Cai et al. [63]. On the other hand, the comparison of the vertical E × B drift speed measured in the incoherent radar of Jicamarca (https://www.igp.gob.pe/observatorios/radio-observatorio-jicamarca/madrigal, last accessed on 20 August 2023), shows that the 15 February 2018 solar eclipse does not show great differences with the other days (DoYs 45, 47 and 48 of 2018), so there seem to be no significant effects of the geomagnetic activity in the low latitude ionosphere of South America (see Figure 3). There are no measurements for the 30 April 2022 solar eclipse.

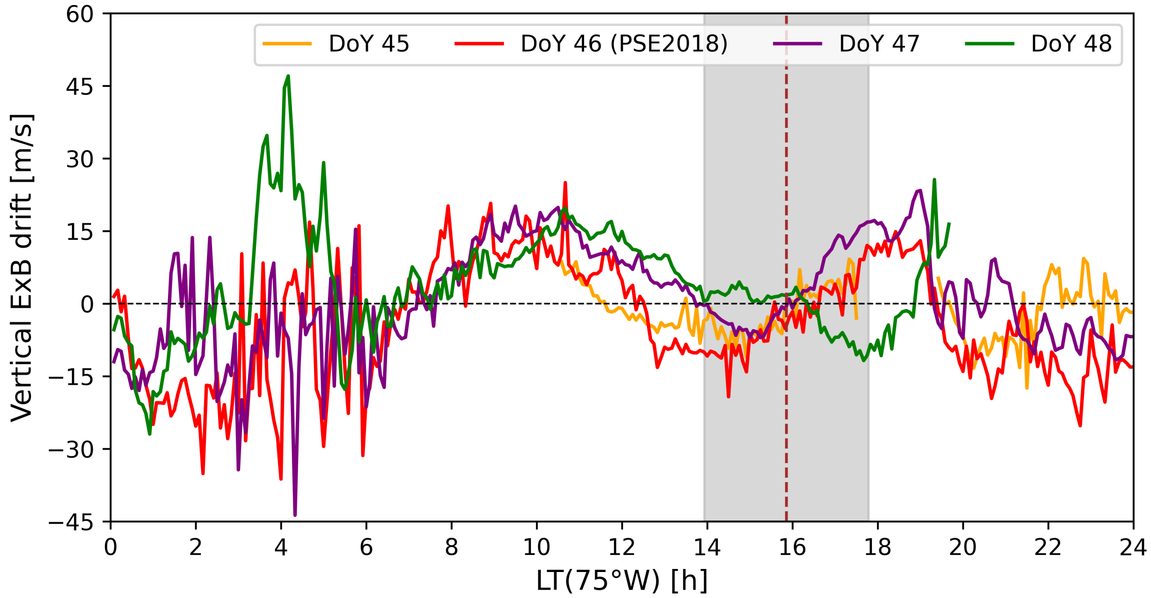

Figure 3. The vertical E × B drift speed measured in the incoherent radar of Jicamarca to compare the eclipse day (DoY 46 of 2018) with respect to DoYs 45, 47, and 48 of 2018. GE (red dashed line) and P1 to P4 (light grey bar) are shown.

2.4.1. Geomagnetic and Solar Activity during Other Eclipses

We also consult the USAF/NOAA Reports of Solar and Geophysical Activity to TSE2019, TSE2020, and TSE2021 (https://www.swpc.noaa.gov, last accessed on 20 August 2023). Solar activity had low levels during these three solar eclipses. The geomagnetic field showed quiet levels during TSE2019 and TSE2020. On 4 December 2021 (TSE2021), the geomagnetic field reached quiet to unsettled levels, where the AE index and Vsw had some activity levels. AE index presented a value of ∼600 nT around 2 UT, decreased until 7 UT, and then it increased (AE index ∼450 nT) until 9 UT. Vsw reached a peak of 534 km/s at ∼3 UT, and it remained above 450 km/s throughout the day.

2.4.2. Earthquake Occurrence

The frequent occurrence of large earthquakes (EQs) on the west coast of South America is due to the fact that this region is on top of the subducting Nazca plate [64]. Therefore, we also investigated whether superficial EQs (depths less than 70 km) with moment magnitudes (M_w) greater than 5 occurred from 10 to 21 February 2018 (by PSE2018), and from 25 April to 6 May 2022 (by PSE2022). This review is relevant because EQs are another important ionospheric disturbance source. We were able to observe that 38 and 30 earthquakes occurred during the analyzed days of 2018 and 2022, respectively (https://earthquake.usgs.gov, last accessed on 25 July 2023). During the days analyzed, however, none of them had a significant influence on the ionospheric behavior across our region of interest.

2.5. Occurrence of Other Ionospheric Disturbance Sources

The occurrence of other ionospheric disturbance sources, such as volcanic eruptions and tsunamis (https://www.ncei.noaa.gov, last accessed on 20 August 2023), was not reported during DoYs 41 to 52 of 2018 and DoYs 115 to 126 of 2022. Also, rocket launches into space from Asia were reported on days 43 and 44 of 2018. On DoYs 117, 119, 120, 122, and 125 of 2022, rocket launches into space from Florida (United States), China, Russia, and New Zealand (https://space.skyrocket.de, last accessed on 20 August 2023) were reported. Then, these rocket launches were far from the region of interest for our study. It is known that thunderstorms/lightning can introduce ionosphere gravity waves

(IGWs) [65,66], but waves in the ionosphere are beyond the scope of our research objective. Therefore, we did not verify the occurrence of thunderstorms/lightning.

3. Results

Here, we provide the main results obtained for PSE2018 and PSE2022. The results found in this paper may be classified as follows: (1) the analysis of ionospheric behavior and TEC maps using GPS stations at a regional scale; and (2) in order to verify our observations with GPS stations, we compare them with Low Earth Orbit (LEO) satellite measurements of the sector involved.

3.1. TEC Changes and Ionospheric Maps Using GPS Stations

Figures 4 and 5 show the summaries of ionospheric maps by comparing the eclipse (VTECe) and the reference days ($\overline{VTEC}$) for PSE2018 and PSE2022, respectively. Eclipse masks are represented from 5% obscuration at 350 km altitude (magenta lines). For both eclipses, we present some particular hours: P1 − 1 h, P1, GE − 0.5 h, GE, GE + 0.5 h, and P4.

Figure 4 illustrates the ionospheric TEC behavior during PSE2018; where 17.95 UT (P1 − 1 h maps), 18.93 UT (P1 maps), 20.36 UT (GE − 0.5 h maps), 20.86 UT with MPO ∼60% (GE maps), 21.36 UT (GE + 0.5 h maps), and 22.79 UT (P4 maps). To see TEC maps from other hours, please go to Supplementary Materials Videos S1 and S2.

From 16.85 UT, we could see that TEC is mostly positive relative to the background TEC (DVTEC ∼50%) between 30°S and 90°S, and it was ±15% between 30°S and 0° latitude. This TEC enhancement can be clearly seen at 17.95 UT (P1 − 1 h maps). The P1 maps (∼18.93 UT) show that the DVTEC value decreases slightly between 30°S and 90°S, where it was ∼20% in this southern South America region. At 19.50 UT, there is a decrease in TEC (DVTEC ∼−20%) in the Antarctica region between 45°W and 135°W longitude. At 20.15 UT, a notable TEC decrease begins around the southern EIA crest over South America around 30°S, 60°W. This TEC change continues to lower its value (DVTEC ∼−50%) and expand its region over South America as time passes. This phenomenon can be observed in the GE − 0.5 h (20.36 UT), GE (20.86 UT), GE + 0.5 h (21.36 UT), and P4 (22.79 UT) maps. From 20:50 UT, there is a shift in TEC decrease relative to the background TEC from the southeast (Antarctic sector) that passes through South Georgia and the South Sandwich Islands in the southern Atlantic Ocean and reaches southern South America at about 20.86 UT (GE maps, where MPO ∼60%). DVTEC remained positive over the studied sector of the Antarctic Peninsula until ∼20.65 UT. In the Antarctic sector, TEC is negative relative to background TEC, and the minimum DVTEC was ∼−40% at 20.65 UT. At about 20.86 UT (see GE maps), we see the DVTEC depletion move from southwest Antarctica to the northeast, and it reaches southern South America. Additionally, the recovery of TEC and some positive values of DVTEC appear over the Antarctic sector. About 22.80 UT (see P4 maps), we can observe the recovery of TEC in southern Chile and Argentina (up to 45°S latitude), but TEC depletion over South America persisted until after 24 UT. Moreover, after P4, the maximum DVTEC was >40% over the Antarctic region, similar to that before the first contact of the eclipse.

Figure 5 is the same as Figure 4 but shows TEC variations during PSE2022. Figure 5 exhibits some particular hours: 17.75 UT (P1 − 1 h); 18.75 UT (P1); 20.19 UT (GE − 0.5 h); 20.69 UT (GE) with MPO 66%; 21.19 UT (GE + 0.5 h); and 22.63 UT (P4). At least before 16 UT, TEC enhancement was >20% relative to the background over South America (30°S to 60°S). This TEC enhancement is clearly illustrated on the P1 − 1 h and P1 maps. After P1, we could observe a decrease in TEC with <−10% along the Antarctic coasts between 60°W and 120°W. TEC decrease (DVTEC ∼−50%) reaches around Drake Passage (∼60°S, ∼60°W) at 20.45 UT. At 20.70 UT, DVTEC had values of around −40% over southern South America and Antarctica (see GE + 0.5 h maps). The visible TEC decrease (DVTEC < −10%) reaches up to 30°S over South America. The improvement of TEC from the geomagnetic equator to 30°S latitude is reinforced around 21.20 UT, and it is maintained for at least 24 UT (P1 + 0.5 h and P4 maps).

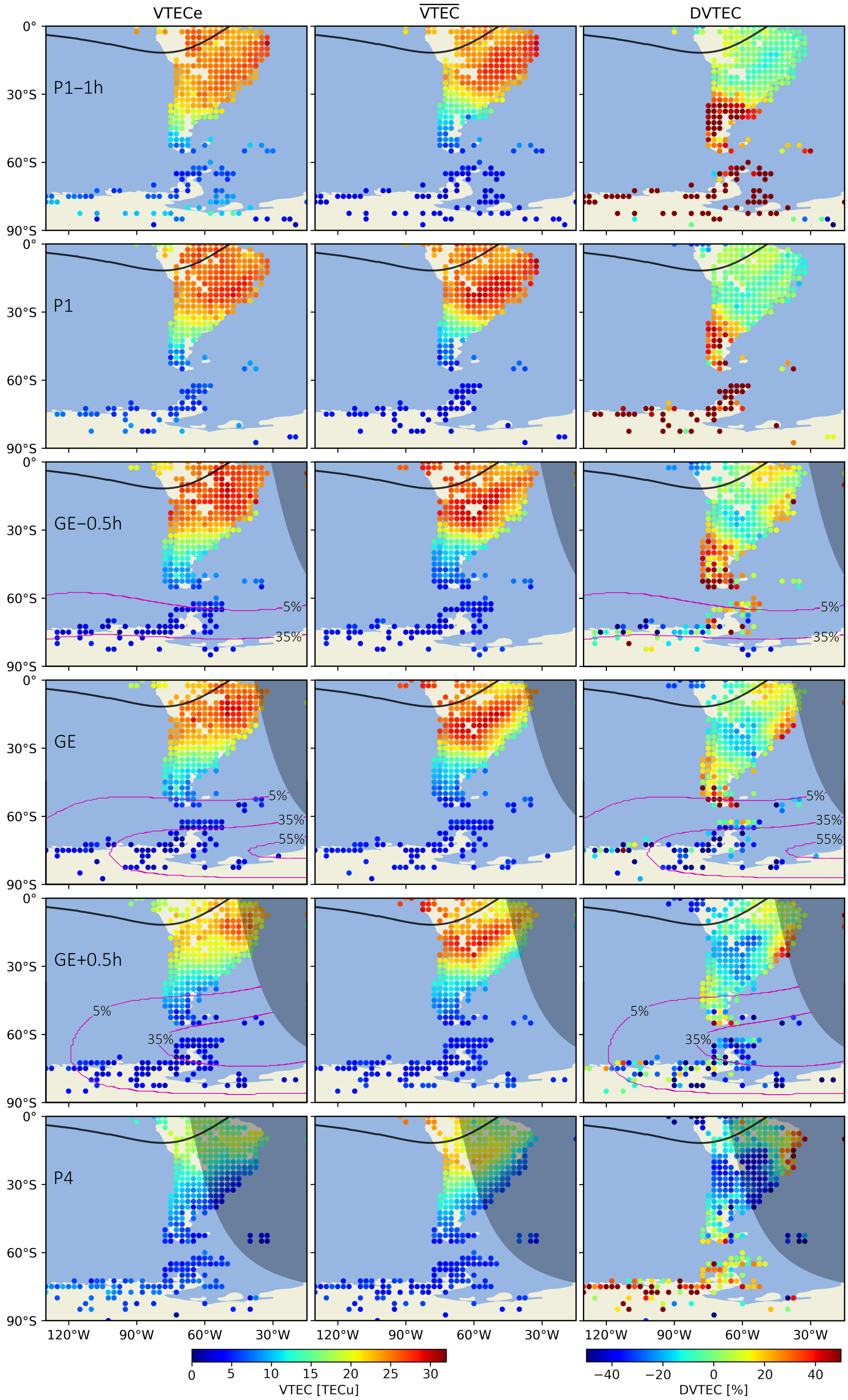

Figure 4. TEC maps during PSE2018 and its eclipse obscuration masks at 350 km ionospheric altitude (magenta lines) are presented. VTECe, $\overline{VTEC}$, and DVTEC (%) are shown from left to right panels. Also, from top to bottom: P1 − 1 h (17.95 UT); P1 (18.93 UT); GE − 0.5 h (20.36 UT); GE (MPO ∼60% at 20.86 UT); GE + 0.5 h (21.36 UT); and P4 (22.79 UT).

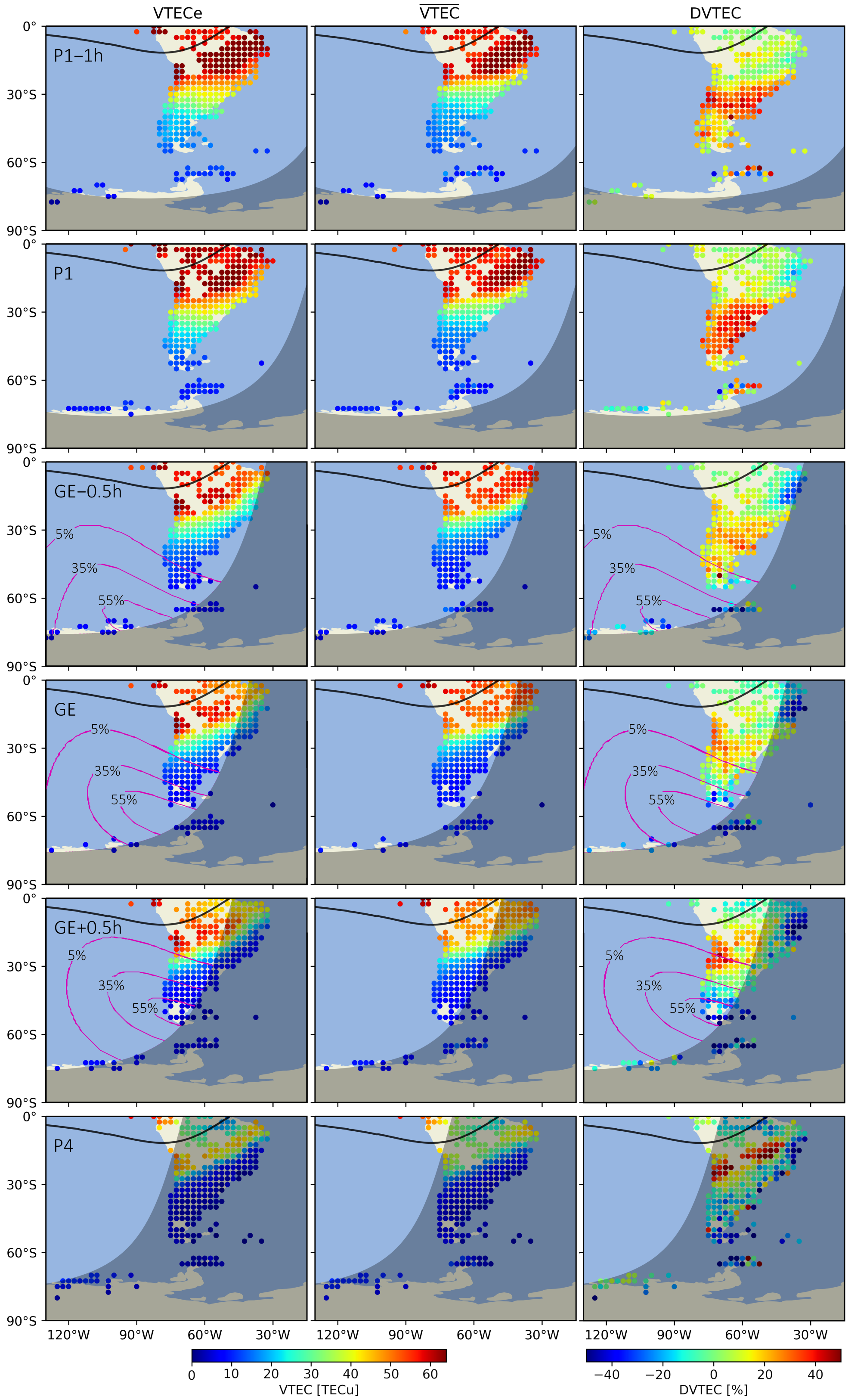

Figure 5. TEC maps during PSE2022 and its eclipse obscuration masks at 350 km ionospheric height (magenta lines) are shown. VTECe, $\overline{VTEC}$, and DVTEC (%) are represented from left to right panels. Additionally, from top to bottom: P1 − 1 h (17.75 UT); P1 (18.75 UT); GE − 0.5 h (20.19 UT); GE (MPO ~66% at 20.69 UT); GE + 0.5 h (21.19 UT); and P4 (22.63 UT).

To study the effects of the PSEs, we chose six GPS stations located in Chile from among more than 390 GPS stations (see Figure 1), where five stations were under the partial region during both eclipses (LSCH, RCSD, IMCH, QLLN, XPLO, CSOM). Additionally, CYHT station was under the shadow of PSE2022, but it was not under the shadow of PSE2018. Table 1 contains more information about the eclipse conditions and the GPS stations to the ionospheric height of 350 km.

Figure 6 shows the results of the TEC behavior of six selected GPS stations for the eclipse day (VTECe), the reference days ($\overline{VTEC}$), and the results of DVTEC (%). We presented each plot between 12 UT and 24 UT. The brown dotted line presents GE time, and it is inside the light blue bar shading the region between P1 and P4. The black dotted line shows MOT; this line is inside the yellow bar between C1 and C4. Both eclipses occurred during the afternoon at six selected stations. We could clearly see the depletion of TEC during both eclipses. The six selected GPS stations had a recovery between 1.5 UT and 2.5 UT the day after both partial eclipses. Table 1 presents the minimum values of DVTEC for each of the six chosen GPS stations.

On the days of PSE2018 and PSE2022, TEC with respect to the background TEC was -29% ($\tau \sim 7$ to 43 min) and -50% ($\tau \sim 1$ to 45 min), respectively. Although CHYT was not under the shadow of PSE2018, it had a noticeable minimum DVTEC (-28%, -6 TECu) at 22.65 UT, after 5 min that LSCH and after 107 min to GE time. Regarding PSE2022, CHYT did not show a clear TEC reduction near MOT at this station. LSCH had minimum DVTEC values greater than 0% and 0 TECu, but it showed an evident TEC depletion near MOT.

We also estimated DVTEC using the first day before and the first day after the PSE2022 as reference days (DoYs 119 and 121 of 2022) due to the ionospheric behavior of the CHYT and LSCH stations, when we took the fifth day before and the fifth day after this eclipse as reference days (DoYs 115 and 125 of 2022), where DoYs 119 and 121 showed values of Kp $> 2^+$ and Vsw > 450 km (see Figure 2). On this occasion, the eclipse-induced effects were shown clearly at CHYT (DVTEC = 0%, -0.2 TECu, and τ = 57 min) and LSCH (DVTEC = -25%, -4.1 TECu, and τ = 32 min). The minimum DVTEC of CHYT occurred 5 min before the end of the partial eclipse in this station. From the ionospheric response due to the eclipse, using reference days DoYs 115 and 125 of 2022 with respect to employment as reference days DoYs 119 and 121 of 2022, we were able to observe that the GPS stations (IMCH, QLLN, and CSMO) located from $\sim$38°S geographic latitude to the south showed a difference in the minimum percentage of DVTEC of less than 11% and a difference of $\tau \pm 5$ min.

The six selected GPS stations showed that the ionosphere was impacted by geomagnetic forcing on the days of the 2018 and 2022 eclipses. On the day of the 2018 eclipse, we can analyze the ionospheric changes from 16 UT. Then, we can observe that the DVTEC of the six GPS stations reaches values from $\sim$10% to $\sim$60% (CHYT: 9%, 2 TECu; LSCH: 28%, 5 TECu; RCSD: 46%, 7 TECu; IMCH: 43%, 6 TECu; QLLN: 58%, 6 TECu; CSOM: 58%, 4 TECu) at around 18 UT (see Figure 6). On the day of the 2022 eclipse, the six selected GPS stations had maximum ionospheric values from 42% to 146% with respect to the reference days. Between P1 time and before we could observe the effects of the eclipse on the ionosphere, DVTEC had a maximum value in each of the six stations (CHYT: 24%, 11.7 TECu; LSCH: 34%, 5.9 TECu; RCSD: 34%, 6.6 TECu; IMCH: 34%, 5.2 TECu; QLLN: 21%, 2.9 TECu; and CSOM: 13%, 1.2 TECu) (see Figure 6).

Table 1. Ionospheric TEC changes and eclipse conditions for each of the six chosen GPS stations. According to [35], we estimated the maximum percentage of obscuration (MPO), start of partial (C1), maximum obscuration time (MOT), and end of partial (C4) eclipses at 350 km altitude.

GPS Station			PSE2018							PSE2022						
Code	**Lat [°S]**	**Lon [°W]**	**MPO [%]**	**C1 [UT]**	**MOT [UT]**	**C4 [UT]**	**τ [min]**	**DVTEC [%]**	**DVTEC [TECu]**	**MPO [%]**	**C1 [UT]**	**MOT [UT]**	**C4 [UT]**	**τ [min]**	**DVTEC [%]**	**DVTEC [TECu]**
CHYT	18.37	70.34	0	0	0	0	12 [a]	−28	−6	8	21.38	22.07	22.70	N.O. [b]	N.O. [b]	N.O. [b]
LSCH	29.91	71.25	3	22.00	22.45	22.87	7	−29	−4.5	30	20.70	21.77	22.73	29	9	1
RCSD	33.65	71.61	6	21.73	22.33	22.90	17	−20	−2.7	38	20.52	21.67	22.68	1	−28	−2.8
IMCH	38.41	73.89	11	21.43	22.18	22.88	35	−12	−1.3	47	20.25	21.48	22.58	20	−37	−2.8
QLLN	43.11	73.66	17	21.15	22.02	22.82	43	−4	−0.4	53	20.07	21.33	22.47	17	−50	−3.6
CSOM	52.78	69.22	32	20.67	21.68	22.63	8	−2	−0.1	62	19.78	21.05	22.18	45	−56	−3.7

[a] In CHYT, τ does not refer to MOT of CHYT, but it refers to MOT of LSCH station. [b] N.O.: We do not observe ionospheric changes near the eclipse time window over the GPS station.

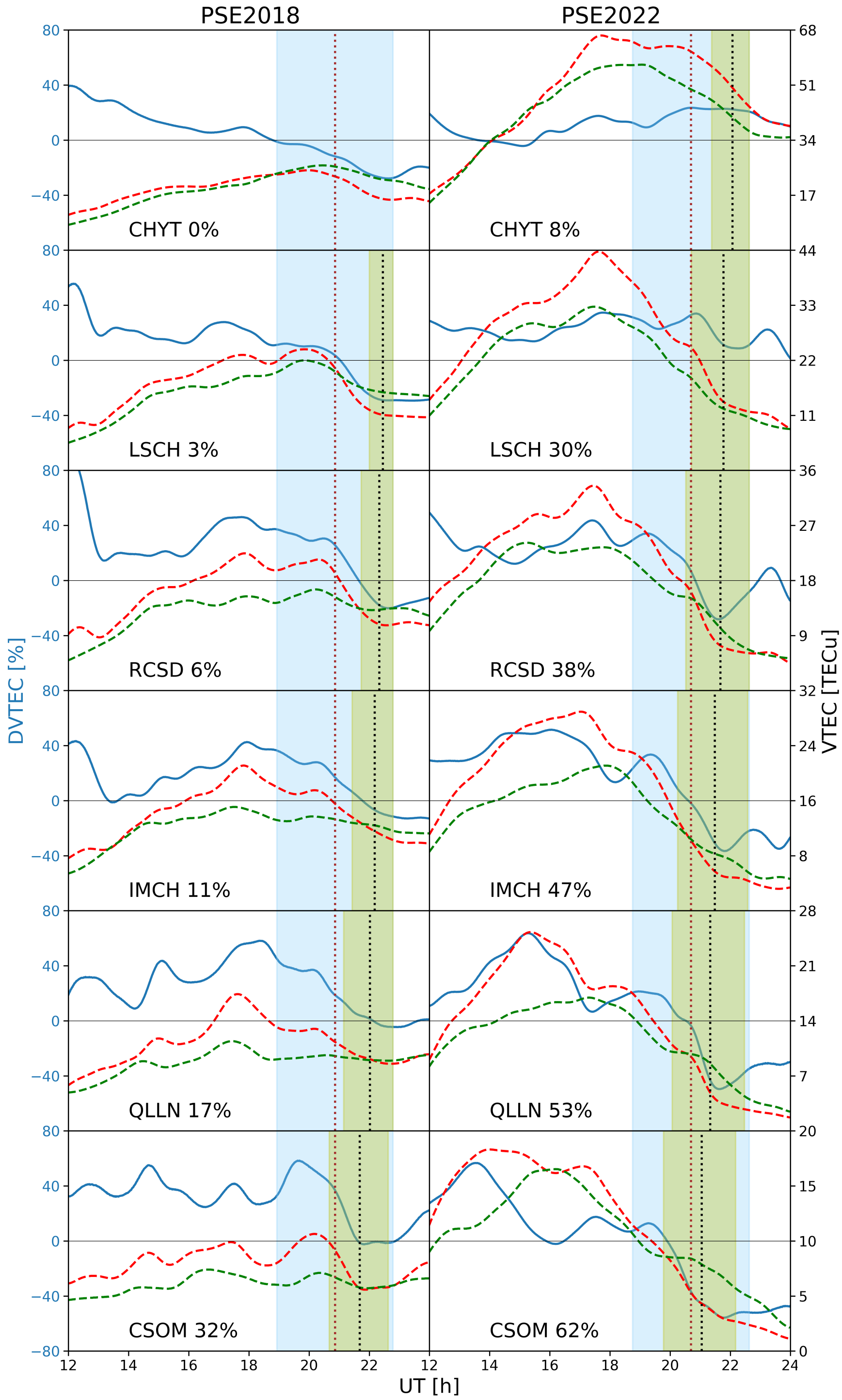

Figure 6. TEC behavior during PSE2018 (**left panel**) and PSE2022 (**right panel**) in selected stations. GPS stations are ordered by latitude. MPO is presented next to each station name. VTECe (red dashed line), $\overline{VTEC}$ (green dashed line), and DVTEC (%) (blue line) are represented. GE (red dotted line), MOT (black dotted line), C1–C4 (yellow bar), and P1–P4 (light blue bar) are also shown.

3.2. Ionospheric Changes Using LEO Satellite Measurements

Figures 7 and 8 show the high ionospheric values in low latitudes and part of the middle latitudes, around the region where the southern EIA crest is located, measured by the SwA and F18 satellites. Figure 7 illustrates the ionospheric behavior for PSE2022 using SwA measurements. We do not show the ionospheric data of PSE2018 because the satellite passes do not cover the region of interest during the eclipse. Then, we present

GPS-VTEC at 850 km altitude (400 km above SwA), and in situ N_e and T_e measurements made by SwA Langmuir probes (at 450 km ionospheric height) on DoY 120 compared to two geomagnetic quiet days (DoYs 115 and 125). We chose the four SwA passes that best fit the eclipse region and eclipse time window over our region of interest (51°W, 74°W, 98°W, and 121°W). Two consecutive descending passes of SwA, the first 74°W (between 20°S and 0°), and the second 98°W (between 30°S and 20°S), show the clear increase in the values of the southern EIA crest (e.g., maximum DVTEC $\sim$ 65% and >10 TECu).

We were able to observe ionospheric effects under the penumbra centered between 70°S and 30°S. Although Figure 7 cannot be easily seen, we present our findings below where the first SwA pass (51°W) took place more than an hour before P1 (18.75 UT), where TEC changes were from −13% to 20% (from −0.3 to 0.8 TECu); DN_e were from 17% to 64% (from 0.09×10^5 el/cm^3 to 0.68×10^5 el/cm^3); and DT_e had fundamentally around −5%, with respect to the background ionospheric values. The second pass (74°W) was close to P1. The minimum DVTEC was −30% (−1 TECu) at 54.0°S at 18.74 UT. The minimum DN_e was −4% (-0.03×10^5 el/cm^3) at 49.4°S at 18.72 UT; and the minimum DT_e was −34% (from $\sim$3100 K to $\sim$2100 K) at 48°S, in relation to the baseline values. The third satellite pass (98°W) occurred minutes prior to GE (20.69 UT). The minimum DVTEC was −52% (−1.5 TECu) at 64.6°S at 20.34 UT. The minimum DN_e was −45% (-0.34×10^5 el/cm^3) at 57°S at 20.3 UT; and the minimum DT_e was −22% (from $\sim$3200 K to $\sim$2500 K) at $\sim$54°S, with respect to the background values. The fourth selected pass of SwA (121°W) happened before P4 (22.63 UT). The minimum DVTEC was −45% (−2.1 TECu) at 54.2°S at 21.84 UT. The minimum DN_e was −31% (-0.36×10^5 el/cm^3) at 40.5°S at 21.78 UT; and the minimum DT_e was −14% (from 3600 K to 3100 K) at $\sim$53°S, regarding background values. Also, DT_e had values fundamentally around ±100 K.

On the other hand, to study the ionospheric changes during PSE2018, we used in situ N_e measurements from two passes of the F18 satellite over the region of interest (see Figure 8a,b). We compare the ionospheric behavior of the day of the eclipse of 2018 (DoY 46) with respect to the mean N_e of the two geomagnetically quiet days (DoYs 41 and 51). The first satellite pass took place from 13°W to 35°W between 20.63 UT and 20.82 UT, a few minutes before GE (20.86 UT), where the N_e values were greater than 10% in the entire evaluated interval (from 70°S to 30°S). The second F18 pass occurred from 38°W to 61°W between 22.33 UT and 22.52 UT, minutes prior to P4 (22.79 UT). The minimum DN_e was −21% (-0.04×10^5 el/cm^3) around 48°S at 22.44 UT.

Regarding the ionospheric fluctuations during PSE2022, we also used three F18 ascending trajectories (see Figure 8c,d). Similar to F18 measurements of PSE2018, we compare the ionospheric changes of the eclipse day of 2022 (DoY 120) with respect to the mean N_e of two previously selected geomagnetically quiet days (DoYs 115 and 125). Before GE (20.69 UT), the satellite passed from 29°W to 51°W, between 19.73 UT and 19.93 UT. N_e remained positive from $\sim$60°S to $\sim$43°S, its value reached $\sim$20% at $\sim$58°S. The DN_e values were less than 0% from 43°S to the North, with a minimum value equal to −10% (-0.02×10^5 el/cm^3) at $\sim$31°S. F18 traveled from 54°W to 77°W between 21.43 UT and 21.63 UT, about an hour after GE (20.69 UT), where the minimum DN_e was −54% (-0.07×10^5 el/cm^3) at 54°S. The third selected pass of this satellite took place from 79°W to 102°W, (23.13 to 23.33 UT), after P4 (22.63 UT). It had a minimum DN_e equal to −30% (-0.06×10^5 el/cm^3) at 40°S.

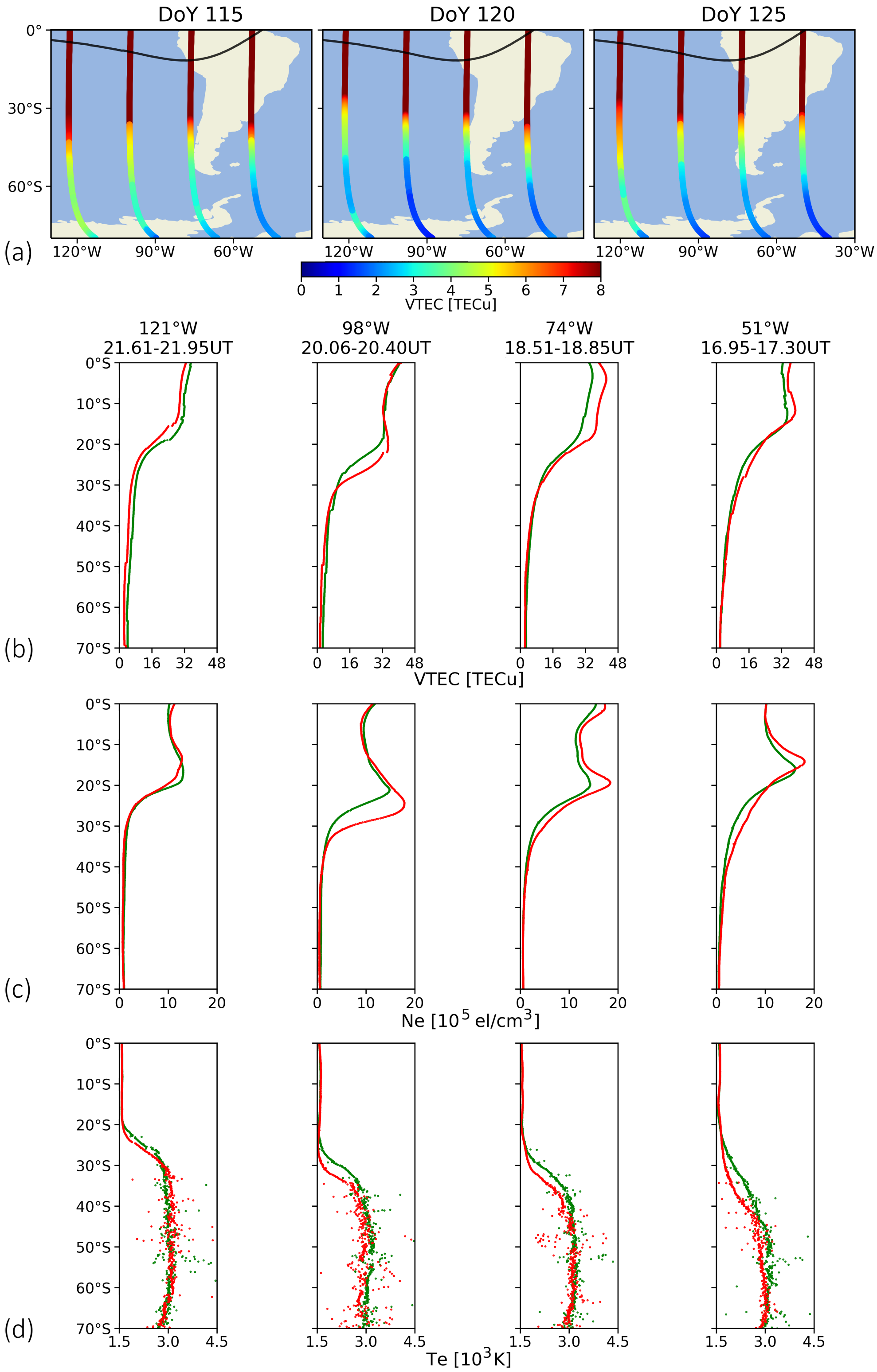

Figure 7. Ionospheric behavior using SwA measurements for PSE2022. (**a**) VTEC data gathered through the satellite orbits taken by SwA at 850 km (400 km above SwA) are presented over the maps during the eclipse day (DoY 120) and the two selected geomagnetically quiet days (DoYs 115 and 125). The black line indicates the magnetic equator. (**b**) Comparison of the latitudinal VTEC profile on the eclipse day (red line) with the mean VTEC of two closest trajectories longitudinally and temporally (DoYs 115 and 125, green line) between 70°S and 0°. (**c**) In situ N_e and (**d**) T_e measurements at 450 km are presented in the same way as VTEC data. The longitudes and time intervals of the satellite passes are also indicated.

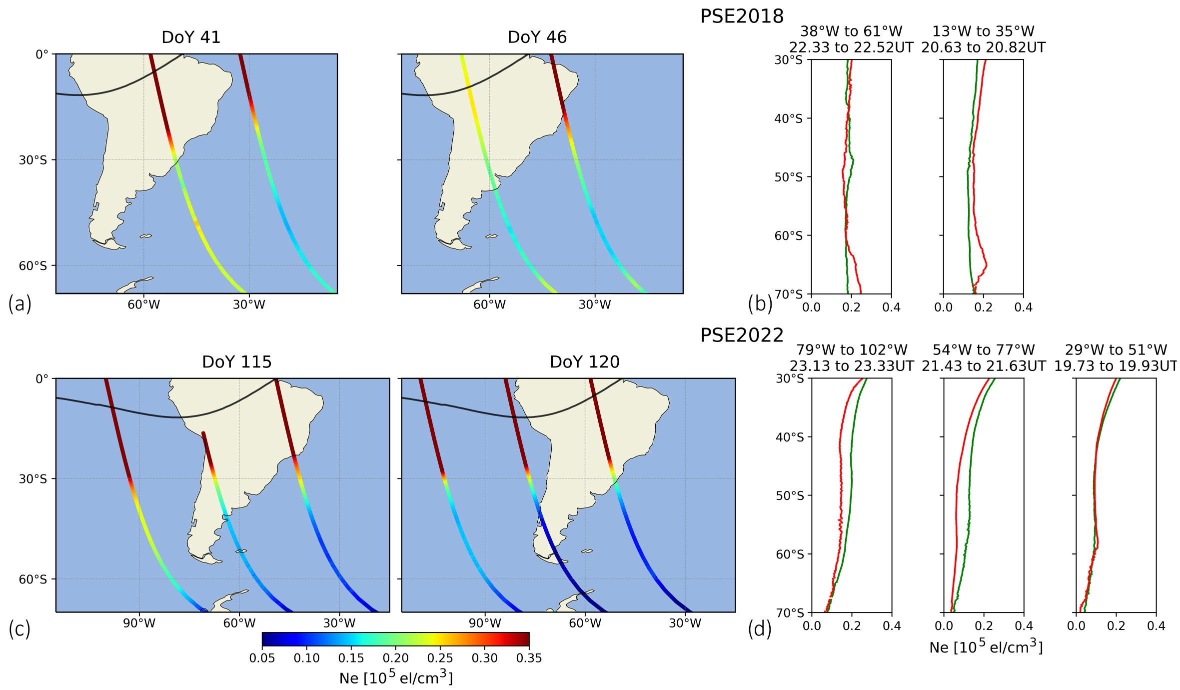

Figure 8. In situ electron density (N_e) data measured by DMSP 5D-3 F18 in the topside ionosphere at about 850 km height for PSE2018 (**a**,**b**) and PSE2022 (**c**,**d**). (**a**,**c**) N_e acquired via satellite orbit the magnetic equator (black line) are displayed on Earth maps. (**b**,**d**) Profile data on eclipse DoYs (DoY 46 of 2018; and DoY 120 of 2022; in red lines) compared with the mean N_e of the reference DoYs (DoYs 41 and 51 of 2018; and DoYs 115 and 125 of 2022, in green lines). The longitudes and time intervals of the satellite passes are also indicated.

4. Discussion

In this part, we examine our main results for both partial solar eclipses. At 350 km ionospheric altitude, the 15 February 2018 and 30 April 2022 eclipses had MPO of 60% and 66%, respectively. The main goals were to present and compare the TEC behavior of both eclipses over South America and the Antarctic sector. The relevance of these events is that there are few that cross over the south polar region (Antarctica) and culminate in the South American region. Moreover, we compare our ionospheric response to earlier findings for total solar eclipses over South America (TSE2019, and TSE2020) and Antarctica (TSE2021).

4.1. F10.7 and TEC

The background TEC values during the EPS2022 period are notably higher than the background TEC values of the EPS2018 period. A possible explanation for this phenomenon is that the solar flux (F10.7) indices during PSE2022 (F10.7 were from 110.6 to 158.5 sfu) are higher than during PSE2018 (F10.7 were from 66.3 to 76.6 sfu), as shown in Figure 2. Additionally, PSE2022 occurred ∼2.5 years after the start of Solar Cycle 25, while PSE2018 occurred less than 2 years before the end of Solar Cycle 24 (see Figure 9). TEC changes are synchronized with solar cycles. Moreover, the dependency between solar index parameters (e.g., solar flux, extreme ultraviolet radiations, and sunspot number) and TEC has been studied by many researchers (e.g., [67,68]). Therefore, we prefer to conduct the percentage analysis of TEC changes to compare the eclipses instead of using TECu.

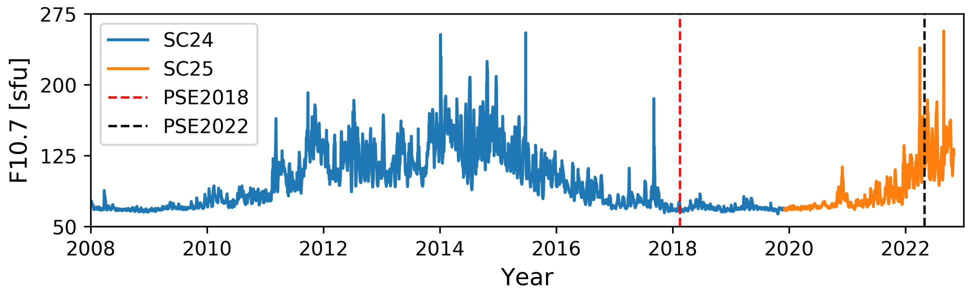

Figure 9. The observed F10.7 Radio Flux during Solar Cycle 24 (SC24, blue line) and Solar Cycle 25 up to day 304 of 2022 (SC25, orange line). 15 February 2018 partial solar eclipse (PSE2018, red dashed line) and 30 April 2022 partial solar eclipse (PSE2022, black dashed line) are also shown.

4.2. Ionospheric TEC Behavior

PSE2018 occurred in a region where we had access to a low density of GPS station measurements. Despite the fact that the PSE2018 and PSE2022 occurred on days with geomagnetic activity (PSE2018: Kp = 5^- and AE = 495 nT; PSE2022: Dst = −37 nT, Kp = 4^+, Vsw = 507 km/s, and AE > 500 nT), we can observe the evident TEC depletions under the Moon's shadow with respect to the background ionosphere (see Figures 4–8 and Table 1). PSE2018 and PSE2022 had similar ionospheric behaviors under the lunar shadow with clear TEC decreases (<−40%) that moved from Antarctica to South America (see Figures 4 and 5). Despite the fact that the maximum obscuration in both eclipses is around 60% at 350 km altitude, the DVTEC values we obtained were consistent with the values presented for the total solar eclipses over South America [6,10,11,13,27,31,43,45,46,48] and Antarctica [49]. Also, τ values were between 1 and 45 min, and the ionospheric effects caused by PSE2018 and PSE2022 persisted after 24 UT because the concentration of electrons does not return to normal levels (see Figure 6 and Table 1). Therefore, the duration (ΔT) of ionospheric changes was over 5 h. This is in agreement with other studies; for example, [34,69] showed that the ionospheric disturbances caused by an eclipse can last more than 7 h. Additionally, the impacts of eclipses can also be seen on a global scale [4,17,34,70] due to the abrupt temperature change and pressure difference brought on by the eclipses-induced rapid cooling of the atmosphere, which may result in AGWs and associated TADs and/or TIDs [4,70]. A thorough examination of these issues, however, is outside the purview of the present paper. Also, the magnetosphere–ionosphere system's electrodynamic interaction caused the polar region under eclipse to cause geospace disturbances that had a larger impact on the ionosphere globally [17].

During PSE2022, we could observe a clear VTEC decrease (−28%, −2.8 TECu) over RCSD (33.65°S, 71.61°W) (see Table 1 and Figure 6). Our results were consistent with the ionospheric behavior (DVTEC = −3 TECu) over Santiago (33.44°S, 70.67°W) reported in [51], for the same eclipse. The ionosphere behavior of the anomaly could be observed at the CHYT and LSCH because these GPS stations are located under the southern EIA crest (see Figures 1, 4 and 5 and Table 1). We could only clearly see the effects induced by the 2022 eclipse at CHYT and LSCH stations when we used non-quiet days as reference days. For example, due to the geographic location of the CHYT station and the geomagnetic activity, this GPS station did not show significant ionospheric variations during the 2022 eclipse when we used selected quiet days as reference days.

We previously showed that the recombination of ionospheric ions and electrons in the absence of sunlight decreased the ionospheric conductivity when the Moon's shadow crossed the ionosphere over South American and Antarctic regions during PSE2018 and PSE2022. However, the enhancement of the ionosphere characterized the geomagnetically active levels on the days of both partial eclipses (see Figures 2 and 4–6). On 15 February 2018, before the P1 time of the PSE2018, we could observe an ionospheric enhancement over the six GPS stations (DVTEC ∼ 10% to ∼60%) near the time that levels of geomagnetic activity were reached at around 18 UT (Kp = 5^- and AE = 495 nT, see Figure 2).

The influence of geomagnetic activity on changes in the ionosphere TEC was observed most clearly at mid and high latitudes (see Figure 4), but there were no significant effects of the geomagnetic activity in the low-latitude ionosphere over South America (see Section 2.4 and Figure 3). Therefore, GPS stations at higher latitudes (in South America), although they had a higher percentage of obscuration, showed less influence on the effects of the eclipse than GPS stations at lower latitudes with a lower percentage of obscuration (see Table 1 and Figures 4 and 6).

The days prior (since DoY 117) to PSE2022 showed some levels of geomagnetic activity. On 30 April 2022, the ionospheric behavior (DVTEC $> 40\%$) observed in the six selected GPS stations coincided with the levels of geomagnetic activity between 0 UT and 6 UT (Kp = 4^+, Dst = -37 nT, and Vsw > 480 km/s; see Figure 2). Subsequently, the DVTEC values began to decrease until around 12 UT (after sunrise in Chile), and then the ionospheric TEC started to increase until the eclipse impacts on the ionosphere could be observed. After the P1 time of the PSE2022, we could observe positive values of DVTEC over the six GPS stations between 13% and 34% with respect to the background ionosphere. Our findings related to the improvements in the ionospheric TEC at the six stations during the day of the 2022 eclipse were in agreement with the graphs shown by Idosa and Beshir [51]. Therefore, although geomagnetic forcing impacted the ionosphere [63], causing a positive increase in TEC during levels of geomagnetic activity, we could clearly see the ionospheric depletion during both eclipses.

On the other hand, we were able to observe a TEC depletion of the southern EIA crest during PSE2018 but a TEC enhancement of the same crest during PSE2022 (see Figures 4–7). During the 2018 solar eclipse, we were able to observe a clear ionospheric TEC depletion (DVTEC $\sim -50\%$) in the EIA crest over South America. These TEC changes spread over South America as time passed. Our percentage of TEC depletion matches what [27,48] showed in the southern EIA crest for TSE2020 over South America and the EIA depletion summary for different eclipses (DVTEC ~ -50 to -20%) by [27]. At least the eclipses of 2018 and 2020 happened in the summer hemisphere. Meanwhile, during the 2022 solar eclipse (hemisphere autumn), we can see a notorious TEC enhancement (DVTEC $> 30\%$) relative to the background in the EIA crest over South America. TEC enhancement in the southern EIA crest obtained by us is comparable to that presented by [31] for TSE2019 (winter hemisphere) over South America, and by [28] for the 2019 December 26 annular solar eclipse (winter hemisphere). Also, we can note that all three eclipses occurred during autumn or winter in their respective hemispheres. Therefore, we demonstrate that our findings of ionospheric behavior in the southern EIA crest for the eclipses of 2018 and 2022 are validated by earlier studies. Moreover, previous research suggests that solar eclipses can cause strong oscillations in the zonal electric field and in the neutral wind circulation pattern, causing a pronounced reduction or marked enhancement in the EIA crests [25,28,29,71].

As a possible explanation for these phenomena, we must consider that, in the summer hemisphere, the Sun's rays arrive perpendicular to the surface, generating a temperature gradient that produces the summer-to-winter neutral wind. This neutral wind transports the plasma by ion-drag effect along the magnetic field lines, in the upward/equatorward direction in the summer hemisphere and in the downward/poleward direction in the winter hemisphere. On the other hand, the vertical $E \times B$ drift at the equator carries plasma to high altitudes, wherein the chemical recombination loss rate is lower and the ambipolar diffusion occurs on both sides along the magnetic field lines (fountain effect) carrying to magnetic latitudes where the chemical recombination loss rate is more significant than the production rate [72]. At the summer EIA crest, an accumulation of plasma occurs due to the opposite directions of the neutral wind and ambipolar diffusion (as modeled by [73]); on the contrary, at the winter EIA crest, the neutral wind and the ambipolar diffusion have the same direction, so there is no accumulation of plasma. Since the solar eclipse is only one day in the entire season, the weakening of the neutral wind due to the shadow of the eclipse should decrease summer EIA crest accumulation and increase winter EIA crest accumulation [74]. This process is observed in the southern EIA crest over South America in PSE2018 (summer), PSE2019 (winter), PSE2020 (summer), and PSE2022 (autumn, close to winter).

SwA and F18 Measurements

In order to verify TEC behavior, we corroborated by SwA and F18 measurements. The minima with respect to the background values of DVTEC, DN_e, and DT_e were -52%, -54% to -21%, and $<-20\%$, respectively, under the penumbra of the eclipses of 2018 and 2022. Our DVTEC and DN_e results are consistent with the data provided in prior publications [34,48,75]. Also, our T_e decrease values are consistent with the findings of earlier studies. For example, previous work reported drops in temperature ($T_e \sim -50$ to -20%) under the shadow of the 21 August 2017 total solar eclipse [76–78] and 26 December 2019 annular solar eclipse [28]. The effects on the ionosphere were observed post-eclipse of 2022 with the satellites. We can observe a minimum $DN_e \sim -30\%$ during the third selected pass of F18 $\sim$0.5 h after P4 time. Also, although the pass of SwA for 121°W was over the Pacific Ocean, somewhat away from the shadow of the eclipse of 2022, it had minima DVTEC, DN_e, and DT_e with -45%, -31%, and -14%, respectively. Furthermore, two consecutive passes of SwA showed the notorious increase in the values of the southern EIA crest (DVTEC $\sim$65%) between 30°S and 0°.

5. Conclusions

The 15 February 2018 and 30 April 2022 solar eclipses under geomagnetic activity in different seasons (summer and autumn) were good opportunities to study how the eclipse-induced ionization changes affect the EIA and radio link-based systems such as GPS. In this paper, we presented and compared the ionospheric TEC changes during PSE2018 and PSE2022 over South America and Antarctica. Both partial solar eclipses had trajectories over the southern polar region and southern South America. These two eclipses took place on non-quiet geomagnetic days. We used a regional GPS network located around both regions. We create regional TEC maps using data from GPS ground stations. Furthermore, we present in more detail the behavior of the two eclipses at six GPS stations located in Chile, along the west coast of South America. We also selected quiet days as reference days after analyzing the geomagnetic and geophysical conditions.

We suggest performing the percentage analysis of TEC variations to compare eclipses instead of using TECu because TEC changes are synchronized with solar cycles. Therefore, it should also consider solar index parameters (e.g., solar flux, extreme ultraviolet radiation, and sunspot number) and not only take into account elements such as the eclipse trajectory, seasons, times of the day, locations, synoptic, and geomagnetic conditions.

TEC maps of both eclipses showed noticeable depletions under the Moon's shadow with DVTEC $< -40\%$, τ between 1 min and 45 min, and duration of ΔT over 5 h. Additionally, TEC decreased (DVTEC $\sim -50\%$) in the southern EIA crest over South America during the 2018 eclipse (hemisphere summer), but the ionization presented a significant enhancement (DVTEC $> 20\%$) that prevailed for a number of hours after the end of the 2022 eclipse (hemisphere autumn, close to winter).

We show that, despite ionospheric enhancement induced by geomagnetic activity on the days of the two eclipses, the impact of both eclipses could be seen. The ionospheric behavior that we estimated with GPS receivers was corroborated using observations from the SwA satellite (VTEC, N_e, and T_e), and the F18 satellite (N_e). The minima with respect to the background values of TEC, N_e, and T_e were -52%, -54% to -21%, and $<-20\%$, respectively. Therefore, the ionospheric behavior unequivocally showed that electron activity in that layer decreases during both solar eclipses, as expected. Furthermore, our findings about the ionospheric behavior of the 2018 and 2022 eclipses during geomagnetic activity are in line with earlier reports for other solar eclipses in the same sector under quiet conditions, such as those TSE2019 and TSE2020 (over South America). We also corroborate our ionospheric results over the Antarctic sector with TSE2021 that occurred during unstable geomagnetic levels.

As a continuation of this work on the 2018 and 2022 partial solar eclipses, we propose to carry out analyses on a regional and/or global scale of the following aspects: Improve our study with the use of other instruments such as ionosondes and magnetometers, among others, to analyze the alteration of the equatorial vertical E $\times$ B drift and generation of a disturbed dynamo. The effects of thermospheric responses (e.g., temperature and winds) to the eclipse also need to be considered. These partial eclipses offer a fantastic opportunity to investigate whether their waves (AGWs, TADs, and TIDs) travel from the poles to low latitudes. Additionally, research into how solar eclipses affect the precision of GNSS and other radiocommunication systems will aid in understanding and mitigating these effects.

Supplementary Materials: The following supporting information can be downloaded at: https://www.mdpi.com/article/10.3390/rs15194810/s1, Video S1: PSE2018; Video S2: PSE2022.

Author Contributions: Conceptualization, J.C.V.-A., M.D. and M.B.; methodology, J.C.V.-A. and M.D.; software, J.C.V.-A., M.B. and Y.S.-S.; validation, J.C.V.-A., M.D., M.B. and Y.S.-S.; formal analysis, J.C.V.-A., M.B. and Y.S.-S.; investigation, J.C.V.-A., M.D., M.B. and Y.S.-S.; resources, J.C.V.-A., M.D., M.B. and Y.S.-S.; data curation, J.C.V.-A., M.B. and Y.S.-S.; writing—original draft preparation, J.C.V.-A., M.B. and Y.S.-S.; writing—review and editing, M.D.; visualization, J.C.V.-A., M.D. and Y.S.-S.; supervision, M.D.; project administration, M.D.; funding acquisition, M.D. All authors have read and agreed to the published version of the manuscript.

Funding: This research was funded by the Air Force Office of Scientific Research under award numbers FA9550-18-1-0249 and the ANID-PIA grant ATE220057. This work was also partially funded by the ANID-FONDECYT Regular 1211144, the ANID-FONDEF ID23I 10360, and the ANID/Scholarship Program/Doctorado Nacional/2018–21181599.

Data Availability Statement: The RINEX files were downloaded from CSN, RAMSAC, IBGE, and UNAVCO. The satellite and receiver bias data were provided from CODE. The geomagnetic data were available from OMNIWeb Plus Data Documentation, WDC for Geomagnetism, and the Space Weather Prediction Center of NOAA. The United States Geological Survey Comprehensive Catalog of Earthquakes offered earthquake data. The occurrence of volcanic eruptions and tsunamis data were downloaded from the National Centers for Environmental Information of NOAA. The rocket launches were verified from Gunter's Space Page. The satellite data were downloaded from the European Space Agency Swarm mission and the Massachusetts Institute of Technology Haystack Observatory Madrigal database.

Acknowledgments: The authors would like to sincerely thank the librarians from Biblioteca Central of the Faculty of Physical and Mathematical Sciences, University of Chile, for their support on references.

Conflicts of Interest: The authors declare no conflicts of interest. The funders had no role in the design of the study; in the collection, analyses, or interpretation of data; in the writing of the manuscript, or in the decision to publish the results.

References

1. Afraimovich, E.L.; Astafyeva, E.I.; Demyanov, V.V.; Edemskiy, I.K.; Gavrilyuk, N.S.; Ishin, A.B.; Kosogorov, E.A.; Leonovich, L.A.; Lesyuta, O.S.; Palamartchouk, K.S.; et al. A review of GPS/GLONASS studies of the ionospheric response to natural and anthropogenic processes and phenomena. *J. Space Weather Space Clim.* **2013**, *3*, A27. [CrossRef]
2. Valdés-Abreu, J.C. Degradation of the Global Navigation Satellite System Positioning Accuracy Caused by Ionospheric Disturbance Sources. Ph.D. Thesis, Universidad de Chile, Santiago, Chile, 2023.
3. Rishbeth, H. Solar eclipses and ionospheric theory. *Space Sci. Rev.* **1968**, *8*, 543–554. [CrossRef]
4. Aa, E.; Zhang, S.R.; Shen, H.; Liu, S.; Li, J. Local and conjugate ionospheric total electron content variation during the 21 June 2020 solar eclipse. *Adv. Space Res.* **2021**, *68*, 3435–3454. [CrossRef]
5. Coster, A.J.; Goncharenko, L.; Zhang, S.R.; Erickson, P.J.; Rideout, W.; Vierinen, J. GNSS Observations of Ionospheric Variations During the 21 August 2017 Solar Eclipse. *Geophys. Res. Lett.* **2017**, *44*, 12041–12048. [CrossRef]
6. Eisenbeis, J.; Occhipinti, G. TEC Depletion Generated by the Total Solar Eclipse of 2 July 2019. *J. Geophys. Res. Space Phys.* **2021**, *126*, e2021JA029186. [CrossRef]

7. He, L.; Heki, K.; Wu, L. Three-Dimensional and Trans-Hemispheric Changes in Ionospheric Electron Density Caused by the Great Solar Eclipse in North America on 21 August 2017. *Geophys. Res. Lett.* **2018**, *45*, 10933–10940. [CrossRef]
8. Le, H.; Liu, L.; Yue, X.; Wan, W. The ionospheric behavior in conjugate hemispheres during the 3 October 2005 solar eclipse. *Ann. Geophys.* **2009**, *27*, 179–184. [CrossRef]
9. Lei, J.; Dang, T.; Wang, W.; Burns, A.; Zhang, B.; Le, H. Long-Lasting Response of the Global Thermosphere and Ionosphere to the 21 August 2017 Solar Eclipse. *J. Geophys. Res. Space Phys.* **2018**, *123*, 4309–4316. [CrossRef]
10. Maurya, A.K.; Shrivastava, M.N.; Kumar, K.N. Ionospheric monitoring with the Chilean GPS eyeball during the South American total solar eclipse on 2nd July 2019. *Sci. Rep.* **2020**, *10*, 19380. [CrossRef] [PubMed]
11. Meza, A.; Eylenstein, B.; Natali, M.P.; Bosch, G.; Moirano, J.; Chalar, E. Analysis of Ionospheric and Geomagnetic Response to the 2020 Patagonian Solar Eclipse. *Front. Astron. Space Sci.* **2021**, *8*, 766327. [CrossRef]
12. Mrak, S.; Semeter, J.; Nishimura, Y.; Hirsch, M.; Sivadas, N. Coincidental TID Production by Tropospheric Weather During the August 2017 Total Solar Eclipse. *Geophys. Res. Lett.* **2018**, *45*, 10903–10911. [CrossRef]
13. Shrivastava, M.N.; Maurya, A.K.; Kumar, K.N. Ionospheric perturbation during the South American total solar eclipse on 14th December 2020 revealed with the Chilean GPS eyeball. *Sci. Rep.* **2021**, *11*, 20324. [CrossRef] [PubMed]
14. Stankov, S.M.; Bergeot, N.; Berghmans, D.; Bolsée, D.; Bruyninx, C.; Chevalier, J.M.; Clette, F.; De Backer, H.; De Keyser, J.; D'Huys, E.; et al. Multi-instrument observations of the solar eclipse on 20 March 2015 and its effects on the ionosphere over Belgium and Europe. *J. Space Weather Space Clim.* **2017**, *7*, A19. [CrossRef]
15. Yan, M.; Dang, T.; Lei, J.; Wang, W.; Zhang, S.R.; Le, H. From Bow Waves to Traveling Atmospheric Disturbances: Thermospheric Perturbations Along Solar Eclipse Trajectory. *J. Geophys. Res. Space Phys.* **2021**, *126*, e2020JA028523. [CrossRef]
16. Zhang, S.R.; Erickson, P.J.; Vierinen, J.; Aa, E.; Rideout, W.; Coster, A.J.; Goncharenko, L.P. Conjugate Ionospheric Perturbation During the 2017 Solar Eclipse. *J. Geophys. Res. Space Phys.* **2021**, *126*, e2020JA028531. [CrossRef]
17. Chen, X.; Dang, T.; Zhang, B.; Lotko, W.; Pham, K.; Wang, W.; Lin, D.; Sorathia, K.; Merkin, V.; Luan, X.; et al. Global Effects of a Polar Solar Eclipse on the Coupled Magnetosphere-Ionosphere System. *Geophys. Res. Lett.* **2021**, *48*, e2021GL096471. [CrossRef]
18. Davis, C.J.; Lockwood, M.; Bell, S.A.; Smith, J.A.; Clarke, E.M. Ionospheric measurements of relative coronal brightness during the total solar eclipses of 11 August, 1999 and 9 July, 1945. *Ann. Geophys.* **2000**, *18*, 182–190. [CrossRef]
19. Krankowski, A.; Shagimuratov, I.; Baran, L.; Yakimova, G. The effect of total solar eclipse of October 3, 2005, on the total electron content over Europe. *Adv. Space Res.* **2008**, *41*, 628–638. [CrossRef]
20. Adekoya, B.; Chukwuma, V. Ionospheric F2 layer responses to total solar eclipses at low and mid-latitude. *J. Atmos. Sol. Terr. Phys.* **2016**, *138–139*, 136–160. [CrossRef]
21. Cheng, K.; Huang, Y.N.; Chen, S.W. Ionospheric effects of the solar eclipse of September 23, 1987, around the equatorial anomaly crest region. *J. Geophys. Res. Space Phys.* **1992**, *97*, 103–111. [CrossRef]
22. Tsai, H.; Liu, J. Ionospheric total electron content response to solar eclipses. *J. Geophys. Res. Space Phys.* **1999**, *104*, 12657–12668. [CrossRef]
23. Mayaud, P. The equatorial counter-electrojet—A review of its geomagnetic aspects. *J. Atmos. Terr. Phys.* **1977**, *39*, 1055–1070. [CrossRef]
24. Bhaskar, A.; Purohit, A.; Hemalatha, M.; Pai, C.; Raghav, A.; Gurada, C.; Radha, S.; Yadav, V.; Desai, V.; Chitnis, A.; et al. A study of secondary cosmic ray flux variation during the annular eclipse of 15 January 2010 at Rameswaram, India. *Astropart. Phys.* **2011**, *35*, 223–229. [CrossRef]
25. St.-Maurice, J.P.; Ambili, K.M.; Choudhary, R.K. Local electrodynamics of a solar eclipse at the magnetic equator in the early afternoon hours. *Geophys. Res. Lett.* **2011**, *38*, L04102. [CrossRef]
26. Panda, S.; Gedam, S.; Rajaram, G.; Sripathi, S.; Bhaskar, A. Impact of the 15 January 2010 annular solar eclipse on the equatorial and low latitude ionosphere over the Indian region. *J. Atmos. Sol. Terr. Phys.* **2015**, *135*, 181–191. [CrossRef]
27. Resende, L.C.A.; Zhu, Y.; Denardini, C.M.; Chen, S.S.; Chagas, R.A.J.; Da Silva, L.A.; Carmo, C.S.; Moro, J.; Barros, D.; Nogueira, P.A.B.; et al. A multi-instrumental and modeling analysis of the ionospheric responses to the solar eclipse on 14 December 2020 over the Brazilian region. *Ann. Geophys.* **2022**, *40*, 191–203. [CrossRef]
28. Aa, E.; Zhang, S.R.; Erickson, P.J.; Goncharenko, L.P.; Coster, A.J.; Jonah, O.F.; Lei, J.; Huang, F.; Dang, T.; Liu, L. Coordinated Ground-Based and Space-Borne Observations of Ionospheric Response to the Annular Solar Eclipse on 26 December 2019. *J. Geophys. Res. Space Phys.* **2020**, *125*, e2020JA028296. [CrossRef]
29. Chen, C.H.; Lin, C.H.C.; Matsuo, T. Ionospheric responses to the 21 August 2017 solar eclipse by using data assimilation approach. *Prog. Earth Planet. Sci.* **2019**, *6*, 13. [CrossRef]
30. Guo, M.; Xu, N.; Feng, J.; Deng, Z. A prolonged pattern of the ionospheric depletion in the south of the 21 August 2017 solar eclipse path. *J. Atmos. Sol. Terr. Phys.* **2020**, *199*, 105208. [CrossRef]
31. Jonah, O.F.; Goncharenko, L.; Erickson, P.J.; Zhang, S.; Coster, A.; Chau, J.L.; de Paula, E.R.; Rideout, W. Anomalous Behavior of the Equatorial Ionization Anomaly During the 2 July 2019 Solar Eclipse. *J. Geophys. Res. Space Phys.* **2020**, *125*, e2020JA027909. [CrossRef]
32. Wang, X.; Berthelier, J.J.; Lebreton, J.P. Ionosphere variations at 700 km altitude observed by the DEMETER satellite during the 29 March 2006 solar eclipse. *J. Geophys. Res. Space Phys.* **2010**, *115*, A11312. [CrossRef]
33. Chen, G.; Zhao, Z.; Ning, B.; Deng, Z.; Yang, G.; Zhou, C.; Yao, M.; Li, S.; Li, N. Latitudinal dependence of the ionospheric response to solar eclipse of 15 January 2010. *J. Geophys. Res. Space Phys.* **2011**, *116*, A06301. [CrossRef]

34. Valdés-Abreu, J.C.; Díaz, M.A.; Bravo, M.; Báez, J.C.; Stable-Sánchez, Y. Ionospheric Behavior during the 10 June 2021 Annular Solar Eclipse and Its Impact on GNSS Precise Point Positioning. *Remote Sens.* **2022**, *14*, 3119. [CrossRef]
35. Verhulst, T.G.W.; Stankov, S.M. Height Dependency of Solar Eclipse Effects: The Ionospheric Perspective. *J. Geophys. Res. Space Phys.* **2020**, *125*, e2020JA028088. [CrossRef]
36. Kundu, S.; Chowdhury, S.; Palit, S.; Mondal, S.K.; Sasmal, S. Variation of ionospheric plasma density during the annular solar eclipse on December 26, 2019. *Astrophys. Space Sci.* **2022**, *367*, 44. [CrossRef]
37. Clilverd, M.A.; Rodger, C.J.; Thomson, N.R.; Lichtenberger, J.; Steinbach, P.; Cannon, P.; Angling, M.J. Total solar eclipse effects on VLF signals: Observations and modeling. *Radio Sci.* **2001**, *36*, 773–788. [CrossRef]
38. Kumar, S.; Kumar, A.; Maurya, A.K.; Singh, R. Changes in the D region associated with three recent solar eclipses in the South Pacific region. *J. Geophys. Res. Space Phys.* **2016**, *121*, 5930–5943. [CrossRef]
39. Chakrabarti, S.K.; Sasmal, S.; Chakraborty, S.; Basak, T.; Tucker, R.L. Modeling D-region ionospheric response of the Great American TSE of August 21, 2017 from VLF signal perturbation. *Adv. Space Res.* **2018**, *62*, 651–661. [CrossRef]
40. Ghosh, S.; Chowdhury, S.; Kundu, S.; Biswas, S.; Dawn, A.; Ray, S.; Choudhury, A.K.; Bari, M.W.; Bhowmick, D.; Manna, S.; et al. Observations and modeling of D-region ionospheric response of Annular Solar Eclipse on December 26, 2019, using VLF signal amplitude and phase variation. *Astrophys. Space Sci.* **2023**, *368*, 19. [CrossRef]
41. Aryal, S.; Evans, J.S.; Correira, J.; Burns, A.G.; Wang, W.; Solomon, S.C.; Laskar, F.I.; McClintock, W.E.; Eastes, R.W.; Dang, T.; et al. First Global-Scale Synoptic Imaging of Solar Eclipse Effects in the Thermosphere. *J. Geophys. Res. Space Phys.* **2020**, *125*, e2020JA027789. [CrossRef]
42. Vargas, F.; Liu, A.; Swenson, G.; Segura, C.; Vega, P.; Fuentes, J.; Pautet, D.; Taylor, M.; Zhao, Y.; Morton, Y.; et al. Mesosphere and Lower Thermosphere Changes Associated With the 2 July 2019 Total Eclipse in South America Over the Andes Lidar Observatory, Cerro Pachon, Chile. *J. Geophys. Res. Atmos.* **2022**, *127*, e2021JD035064. [CrossRef]
43. Bravo, M.; Martínez-Ledesma, M.; Foppiano, A.; Urra, B.; Ovalle, E.; Villalobos, C.; Souza, J.; Carrasco, E.; Muñoz, P.R.; Tamblay, L.; et al. First Report of an Eclipse From Chilean Ionosonde Observations: Comparison With Total Electron Content Estimations and the Modeled Maximum Electron Concentration and Its Height. *J. Geophys. Res. Space Phys.* **2020**, *125*, e2020JA027923. [CrossRef]
44. Martínez-Ledesma, M.; Bravo, M.; Urra, B.; Souza, J.; Foppiano, A. Prediction of the Ionospheric Response to the 14 December 2020 Total Solar Eclipse Using SUPIM-INPE. *J. Geophys. Res. Space Phys.* **2020**, *125*, e2020JA028625. [CrossRef]
45. Gómez, D.D. Ionospheric Response to the December 14, 2020 Total Solar Eclipse in South America. *J. Geophys. Res. Space Phys.* **2021**, *126*, e2021JA029537. [CrossRef]
46. De Haro Barbás, B.; Bravo, M.; Elias, A.; Martínez-Ledesma, M.; Molina, G.; Urra, B.; Venchiarutti, J.; Villalobos, C.; Namour, J.; Ovalle, E.; et al. Longitudinal variations of ionospheric parameters near totality during the eclipse of December 14, 2020. *Adv. Space Res.* **2022**, *69*, 2158–2167. [CrossRef]
47. Zhang, K.; Wang, H. The Great Reduction of Equatorial Electrojet During the Solar Eclipse on 14 December 2020. *Space Weather* **2022**, *20*, e2022SW003295. [CrossRef]
48. Bravo, M.; Molina, M.; Martínez-Ledesma, M.; de Haro Barbás, B.; Urra, B.; Elías, A.; Souza, J.; Villalobos, C.; Namour, J.; Ovalle, E.; et al. Ionospheric Response Modeling under Eclipse Conditions: Evaluation of December 14, 2020, Total Solar Eclipse Prediction over the South American sector. *Front. Astron. Space Sci.* **2022**, *9*, 1021910. [CrossRef]
49. Idosa, C.U.; Rikitu, K.S. Effects of Total Solar Eclipse on Ionospheric Total Electron Content over Antarctica on 2021 December 4. *Astrophys. J.* **2022**, *932*, 2. [CrossRef]
50. Coyle, S.; Hartinger, M.D.; Clauer, C.R.; Baker, J.B.H.; Cnossen, I.; Freeman, M.P.; Weygand, J.M. The 2021 Antarctic Total Eclipse: Ground Magnetometer and GNSS Wave Observations From the 40 Degree Magnetic Meridian. *J. Geophys. Res. Space Phys.* **2023**, *128*, e2022JA031142. [CrossRef]
51. Idosa Uga, C.; Beshir Seba, E. Ionospheric response to a moderate geomagnetic storm on 14 April 2022 and a partial solar eclipse 30 April 2022. *Indian J. Phys.* **2023**, *47*, 1–11. [CrossRef]
52. Abidin Abdul Rashid, Z.; Awad Momani, M.; Sulaiman, S.; Alauddin Mohd Ali, M.; Yatim, B.; Fraser, G.; Sato, N. GPS ionospheric TEC measurement during the 23rd November 2003 total solar eclipse at Scott Base Antarctica. *J. Atmos. Sol. Terr. Phys.* **2006**, *68*, 1219–1236. [CrossRef]
53. Chernogor, L.; Garmash, K. Magneto-ionospheric effects of the solar eclipse of March 20, 2015, over Kharkov. *Geomagn. Aeron.* **2017**, *57*, 72–83. [CrossRef]
54. Hoque, M.M.; Wenzel, D.; Jakowski, N.; Gerzen, T.; Berdermann, J.; Wilken, V.; Kriegel, M.; Sato, H.; Borries, C.; Minkwitz, D. Ionospheric response over Europe during the solar eclipse of March 20, 2015. *J. Space Weather Space Clim.* **2016**, *6*, A36. [CrossRef]
55. Panasenko, S.V.; Otsuka, Y.; van de Kamp, M.; Chernogor, L.F.; Shinbori, A.; Tsugawa, T.; Nishioka, M. Observation and characterization of traveling ionospheric disturbances induced by solar eclipse of 20 March 2015 using incoherent scatter radars and GPS networks. *J. Atmos. Sol. Terr. Phys.* **2019**, *191*, 105051. [CrossRef]
56. Verhulst, T.G.W.; Sapundjiev, D.; Stankov, S.M. High-resolution ionospheric observations and modeling over Belgium during the solar eclipse of 20 March 2015 including first results of ionospheric tilt and plasma drift measurements. *Adv. Space Res.* **2016**, *57*, 2407–2419. [CrossRef]
57. Valdés-Abreu, J.C.; Díaz, M.A.; Báez, J.C.; Stable-Sánchez, Y. Effects of the 12 May 2021 Geomagnetic Storm on Georeferencing Precision. *Remote Sens.* **2022**, *14*, 38. [CrossRef]

58. Seemala, G.K.; Valladares, C.E. Statistics of total electron content depletions observed over the South American continent for the year 2008. *Radio Sci.* **2011**, *46*, RS5019. [CrossRef]
59. Estey, L.H.; Meertens, C.M. TEQC: The multi-purpose toolkit for GPS/GLONASS data. *GPS Solut.* **1999**, *3*, 42–49. [CrossRef]
60. Piñón, D.; Gomez, D.; Smalley, B.; Cimbaro, S.; Lauría, E.; Bevis, M. The History, State, and Future of the Argentine Continuous Satellite Monitoring Network and Its Contributions to Geodesy in Latin America. *Seismol. Res. Lett.* **2018**, *89*, 475–482. [CrossRef]
61. Tsidu, G.M.; Abraha, G. Moderate geomagnetic storms of January 22–25. 2012 and their influences on the wave components in ionosphere and upper stratosphere-mesosphere regions. *Adv. Space Res.* **2014**, *54*, 1793–1812. [CrossRef]
62. Nose, M.; Iyemori, T.; Sugiura, M.; Kamei, T. Geomagnetic Dst index. *World Data Cent. Geomagn. Kyoto* **2015**, *10*, 15–31 . [CrossRef]
63. Cai, X.; Burns, A.G.; Wang, W.; Qian, L.; Pedatella, N.; Coster, A.; Zhang, S.; Solomon, S.C.; Eastes, R.W.; Daniell, R.E.; et al. Variations in Thermosphere Composition and Ionosphere Total Electron Content Under "Geomagnetically Quiet" Conditions at Solar-Minimum. *Geophys. Res. Lett.* **2021**, *48*, e2021GL093300. [CrossRef]
64. Easton, G.; González-Alfaro, J.; Villalobos, A.; Álvarez, G.; Melgar, D.; Ruiz, S.; Sepúlveda, B.; Escobar, M.; León, T.; Carlos Báez, J.; et al. Complex Rupture of the 2015 Mw 8.3 Illapel Earthquake and Prehistoric Events in the Central Chile Tsunami Gap. *Seismol. Res. Lett.* **2022**, *93*, 1479–1496. [CrossRef]
65. Liu, T.; Yu, Z.; Ding, Z.; Nie, W.; Xu, G. Observation of Ionospheric Gravity Waves Introduced by Thunderstorms in Low Latitudes China by GNSS. *Remote Sens.* **2021**, *13*, 4131. [CrossRef]
66. Osei-Poku, L.; Tang, L.; Chen, W.; Mingli, C. Evaluating Total Electron Content (TEC) Detrending Techniques in Determining Ionospheric Disturbances during Lightning Events in A Low Latitude Region. *Remote Sens.* **2021**, *13*, 4753. [CrossRef]
67. Chakraborty, S.K.; Hajra, R. Solar control of ambient ionization of the ionosphere near the crest of the equatorial anomaly in the Indian zone. *Ann. Geophys.* **2008**, *26*, 47–57. [CrossRef]
68. Mansoori, A.; Khan, P.; Ahmad, R.; Atulkar, R.; Aslam, A.; Bhardwaj, S.; Malvi, B.; Purohit, P.; Gwal, A. Evaluation of long term solar activity effects on GPS derived TEC. *J. Phys. Conf. Ser.* **2016**, *759*, 012069. [CrossRef]
69. Huang, F.; Li, Q.; Shen, X.; Xiong, C.; Yan, R.; Zhang, S.R.; Wang, W.; Aa, E.; Zhong, J.; Dang, T.; et al. Ionospheric Responses at Low Latitudes to the Annular Solar Eclipse on 21 June 2020. *J. Geophys. Res. Space Phys.* **2020**, *125*, e2020JA028483. [CrossRef]
70. Dang, T.; Lei, J.; Wang, W.; Zhang, B.; Burns, A.; Le, H.; Wu, Q.; Ruan, H.; Dou, X.; Wan, W. Global Responses of the Coupled Thermosphere and Ionosphere System to the August 2017 Great American Solar Eclipse. *J. Geophys. Res. Space Phys.* **2018**, *123*, 7040–7050. [CrossRef]
71. Choudhary, R.K.; St.-Maurice, J.P.; Ambili, K.M.; Sunda, S.; Pathan, B.M. The impact of the January 15, 2010, annular solar eclipse on the equatorial and low latitude ionospheric densities. *J. Geophys. Res. Space Phys.* **2011**, *116*, A09309. [CrossRef]
72. Titheridge, J. Winds in the ionosphere—A review. *J. Atmos. Terr. Phys.* **1995**, *57*, 1681–1714 . [CrossRef]
73. Balan, N.; Bailey, G.J. Equatorial plasma fountain and its effects: Possibility of an additional layer. *J. Geophys. Res. Space Phys.* **1995**, *100*, 21421–21432. [CrossRef]
74. Chou, M.Y.; Wu, Q.; Pedatella, N.M.; Cherniak, I.; Schreiner, W.S.; Braun, J. Climatology of the Equatorial Plasma Bubbles Captured by FORMOSAT-3/COSMIC. *J. Geophys. Res. Space Phys.* **2020**, *125*, e2019JA027680. [CrossRef]
75. Cherniak, I.; Zakharenkova, I. Ionospheric Total Electron Content Response to the Great American Solar Eclipse of 21 August 2017. *Geophys. Res. Lett.* **2018**, *45*, 1199–1208. [CrossRef]
76. Goncharenko, L.P.; Erickson, P.J.; Zhang, S.R.; Galkin, I.; Coster, A.J.; Jonah, O.F. Ionospheric Response to the Solar Eclipse of 21 August 2017 in Millstone Hill (42N) Observations. *Geophys. Res. Lett.* **2018**, *45*, 4601–4609. [CrossRef]
77. Hairston, M.R.; Mrak, S.; Coley, W.R.; Burrell, A.; Holt, B.; Perdue, M.; Depew, M.; Power, R. Topside ionospheric electron temperature observations of the 21 August 2017 eclipse by DMSP spacecraft. *Geophys. Res. Lett.* **2018**, *45*, 7242–7247. [CrossRef]
78. Hussien, F.; Ghamry, E.; Fathy, A.; Mahrous, S. Swarm satellite observations of the 21 August 2017 solar eclipse. *J. Astron. Space Sci.* **2020**, *37*, 29–34. [CrossRef]